Monthly Notices of the ROYAL ASTRONOMICAL SOCIETY

MNRAS **502,** 3021–3034 (2021) doi:10.1093/mnras/stab197
Advance Access publication 2021 January 25

Vibrationally excited HC_3N emission in NGC 1068: tracing the recent star formation in the starburst ring

F. Rico-Villas [1]★ J. Martín-Pintado,[1] E. González-Alfonso,[2] V. M. Rivilla [1,3] S. Martín [4,5] S. García-Burillo,[6] I. Jiménez-Serra[1] and M. Sánchez-García[1]

[1]*Centro de Astrobiología (CSIC-INTA), Ctra de Ajalvir, km 4, Torrejón de Ardoz, E-28850 Madrid, Spain*
[2]*Departamento de Física y Matemáticas, Universidad de Alcalá, Campus Universitario, Alcalá de Henares, E-28871 Madrid, Spain*
[3]*INAF – Osservatorio Astrofisico di Arcetri, Largo Enrico Fermi 5, I-50125 Florence, Italy*
[4]*European Southern Observatory, Alonso de Córdova, 3107, Vitacura, Santiago 763-0355, Chile*
[5]*Joint ALMA Observatory, Alonso de Córdova, 3107, Vitacura, Santiago 763-0355, Chile*
[6]*Observatorio Astronómico Nacional (OAN-IGN) – Observatorio de Madrid, Alfonso XII, 3, E-28014 Madrid, Spain*

Accepted 2021 January 19. Received 2020 November 17; in original form 2020 August 10

ABSTRACT

Using the ALMA data, we have studied the HC_3N and continuum emission in the starburst pseudo-ring (SB pseudo-ring) and the circumnuclear disc (CND) of the SB/active galactic nucleus (AGN) composite galaxy NGC 1068. We have detected emission from vibrationally excited HC_3N (HC_3N^*) only towards one star-forming region of the SB pseudo-ring. Remarkably, HC_3N^* was not detected towards the CND despite its large HC_3N $v = 0$ column density. From local thermodynamic equilibrium (LTE) and non-LTE modelling of HC_3N^*, we obtained a dust temperature ($T_{\rm dust}$) of ∼250 K and a density ($n_{\rm H_2}$) of 6×10^5 cm^{-3} for this star-forming region. The estimated infrared (IR) luminosity of 5.8×10^8 L$_\odot$ is typical of proto-superstar clusters (proto-SSCs) observed in the SB galaxy NGC 253. We use the continuum emissions at 147 and 350 GHz, along with CO and Paα, to estimate the ages of other 14 SSCs in the SB pseudo-ring. We find the SSCs to be associated with the region connecting the nuclear bar with the SB pseudo-ring, supporting the inflow scenario. For the CND, our analysis yields $T_{\rm dust} \leq 100$ K and $n_{\rm H_2} \sim (3–6) \times 10^5$ cm^{-3}. The very different dust temperatures found for the CND and the proto-SSC indicate that, while the dust in the proto-SSC is being efficiently heated from the inside by the radiation from massive protostars, the CND is being heated externally by the AGN, which in the IR optically thin case can only heat the dust to 56 K. We discuss the implications of the non-detection of HC_3N^* near the luminous AGN in NGC 1068 on the interpretation of the HC_3N^* emission observed in the SB/AGN composite galaxies NGC 4418 and Arp 220.

Key words: galaxies: individual: NGC 1068 – galaxies: ISM – galaxies: Seyfert – galaxies: star clusters – galaxies: star formation.

1 INTRODUCTION

In many galaxies, both active galactic nucleus (AGN) and star formation (SF) activity contribute to a significant fraction of the total galaxy luminosity (Genzel et al. 1998). Discerning how much each one contributes to the galaxy luminosity can tell us the physical processes heating the gas and dust and thus evaluate their associated radiative and kinematic feedback in the context of galaxy evolution. In addition, establishing which is the dominating heating mechanism (AGN or SF) in extremely obscured nuclei remains a key problem in extragalactic astrophysics (Martín et al. 2016).

Due to the high extinction in these environments, observations in the infrared (IR) or at shorter wavelengths only detect the outermost surface of the optically thick regions, where column densities of molecular gas can reach values of up to or even beyond $N(H_2) = 10^{25}$ cm^{-2}. With such large column densities, the AGN becomes Compton thick, preventing its identification even in the X-rays (e.g. González-Alfonso et al. 2012; Costagliola et al. 2013; Lusso et al. 2013).

In the last few years, it has been proposed that emission from vibrationally excited molecules such as HCN or HC_3N in highly obscured galactic nuclei can be used as tracers of the nuclear activity in these obscured galaxy nuclei (Costagliola & Aalto 2010; Sakamoto et al. 2010; Martín et al. 2011, 2016; Aalto 2015; Imanishi, Nakanishi & Izumi 2016, 2019; González-Alfonso & Sakamoto 2019). As the radiation from the obscured heating source is reprocessed by the dust into the IR, peaking in the mid-IR (10–50 μm), the IR photons efficiently pump these molecules into their vibrational excited states. On the other hand, the rotational levels from the vibrationally excited molecules emit radiation in the cm to sub-mm wavelength range, unaffected by dust extinction, making them powerful tools to probe the energetic processes taking place in the innermost regions of heavily obscured galactic nuclei.

In particular, vibrationally excited HC_3N (hereafter HC_3N^*) is very well suited for tracing energetic processes in highly obscured regions. In the Milky Way (MW), its emission is associated with warm, dense ultraviolet (UV)-shielded and very compact regions

★ E-mail: fernando.ricovillas@gmail.com

© 2021 The Author(s)
Published by Oxford University Press on behalf of Royal Astronomical Society

Downloaded from https://academic.oup.com/mnras/article/502/2/3021/6119921 by guest on 11 February 2026

around massive star-forming regions, named hot cores (HCs; e.g. Goldsmith et al. 1982; Wyrowski, Schilke & Walmsley 1999; de Vicente et al. 2000, 2002; Martín-Pintado et al. 2005), where HC_3N^* is tracing massive SF in the early protostellar phases (HC and circumstellar phases; Jiménez-Serra et al. 2009). However, HC_3N^* emission is not detected in the circumnuclear disc (CND) surrounding the supermassive black hole (SMBH) of the MW since HC_3N is photodissociated by UV radiation (Costagliola & Aalto 2010; Martín et al. 2012; Costagliola et al. 2015) emitted from the central star cluster.

Outside the MW, HC_3N^* has been observed in the nuclei of very active ultraluminous infrared galaxies (ULIRGs) like NGC 4418 (Costagliola & Aalto 2010; Costagliola et al. 2015) and Arp 220 (Martín et al. 2011). More recently, in Rico-Villas et al. (2020) we detected HC_3N^* emission in the prototypical starburst galaxy NGC 253. Like in the MW, the HC_3N^* emission is related to HCs, but for NGC 253 their associated luminosities were found to be one order of magnitude brighter than those in the MW and consequently being superhot cores (SHCs). In turn, the presence of SHCs is associated with the very early phases of the formation of superstar clusters [i.e. proto-superstar clusters (proto-SSCs)]. SSCs are compact star clusters with ages from ∼1 to 100 Myr and stellar masses of $\gtrsim 10^5\,M_\odot$, which represent an extreme mode of SF. They have been observed mainly in central starbursts of galaxies, ULIRGs, or mergers (see Whitmore & Schweizer 1995; Beck 2015, for a review). Despite the seven proto-SSCs found in NGC 253, in Rico-Villas et al. (2020) we could not identify any HC_3N^* emission associated with the strongest non-thermal source (Turner & Ho 1985) nor its kinematical centre (Müller-Sánchez et al. 2010), both proposed to host an SMBH in this galaxy. Unfortunately, the lack of observational evidence of the presence of an active SMBH in NGC 253 prevented us from studying its possible effects on the vibrational excitation of HC_3N. So far, all the observational data suggest that HC_3N^* emission is mainly tracing the recent brief episodes of massive SF in the very early stages of cluster formation. However, there is not any systematic study of the HC_3N^* emission in nearby galaxies with AGN nuclear activity.

NGC 1068, one of the closest galaxies hosting spatially resolved AGN and starburst (SB) activities, offers a unique opportunity to study the effects of SF and AGN activity from its $\sim 10^7\,M_\odot$ SMBH (Davis et al. 2014; Combes et al. 2019) on the vibrational excitation of HC_3N. NGC 1068 is a prototypical Seyfert 2 barred galaxy, located at $D = 14.4$ Mpc (Bland-Hawthorn et al. 1997), with a luminosity (L_{IR}) of $3 \times 10^{11}\,L_\odot$ (Telesco & Harper 1980). Its central region has been extensively observed to study the AGN activity and its effects of the SMBH on its surroundings, including fuelling and associated feedback. NGC 1068 has an AGN-driven outflow and bipolar radio jets that strongly interact with the interstellar medium (ISM; García-Burillo et al. 2014). In particular, the elliptical ring with $r \sim 200$ pc, known as the CND, surrounding the SMBH is strongly affected by the AGN-driven jets and outflow (Krips et al. 2006; García-Burillo et al. 2014, 2017, 2019; Viti et al. 2014). In addition to the AGN-dominated central region, there is an SB pseudo-ring where most of the recent massive SF of the galaxy concentrates. The SB pseudo-ring is located at $r \simeq 1.3$ kpc from the nucleus and is formed by a two-armed spiral structure that begins at both ends of the central bar (García-Burillo et al. 2014). The SB pseudo-ring is clearly seen in Pa α and CO, contributing significantly to the total CO luminosity of the galaxy (see fig. 1a from García-Burillo et al. 2014, or Fig. 5).

García-Burillo et al. (2014) and Viti et al. (2014) analysed the molecular emission from both the CND and the SB pseudo-ring and found differences in the molecular line ratios (from CO, HCO^+, HCN, and CS) between both regions, indicating that the radiative and mechanical feedback from the AGN has changed the physical conditions and the chemistry of the molecular gas in the CND. They found that, in general, more dense ($10^5\,cm^{-3}$) and warmer ($T \sim 150$ K) gas is found in the CND (Viti et al. 2014), although they only analyse one star-forming region as representative of the SB pseudo-ring. Furthermore, the HC_3N abundance in the CND has been found to be enhanced likely due to the AGN-induced chemistry (Viti et al. 2014), which offers a unique opportunity to study in detail the effects of the SMBH on the heating of its surroundings as traced by the HC_3N^* emission.

In this paper, we study the HC_3N emission in the CND and the SB pseudo-ring of NGC 1068. Despite the bright HC_3N emission from the ground state observed in the CND, we find HC_3N vibrationally excited emission in only one condensation of the SB pseudo-ring, revealing the presence of an SHC. We show that, contrary to massive protostars, the AGN is extremely efficient in heating the gas of the CND mainly through shocks originating in the jet/outflow system, but very inefficient in heating the dust by radiation, which is the requirement for HC_3N to be vibrationally excited for the derived H_2 densities.

2 DATA REDUCTION

To study the HC_3N emission from the SB pseudo-ring and the CND of NGC 1068, we have used publicly available data from the ALMA science archive. The observations are summarized in Table 1. Additionally, we also made use of the *Hubble Space Telescope* NICMOS (NIC3) narrow-band (F187N, F190N) Pa α line emission image of NGC 1068 with an angular resolution of 0.26 arcsec × 0.26 arcsec (for details on the calibration and imaging, see García-Burillo et al. 2014).

The ALMA data calibration and imaging were carried using the Common Astronomy Software Applications (CASA; McMullin et al. 2007) 4.2 version pipeline. Continuum emission maps were obtained by averaging line-free channels. Due to the large amount of molecular emission and the large velocity gradients between the CND and the SB pseudo-ring, data were not continuum subtracted in the *uv*-plane. For deconvolution, we have used the CASA `tclean` task with Briggs weighting setting the `robust` parameter to 0.5. All the produced data cubes and continuum maps were corrected for the primary beam. The achieved synthesized beam sizes and resulting rms noise in the cubes, as well as the corresponding primary beam full width at half-maximum [FWHM; field of view (FOV)], are also listed in Table 1. Since most of the NGC 1068 observations are centred on the AGN position, as we move to higher frequencies the observed FOV of the telescope primary beam is reduced, limiting the observations of the SB pseudo-ring to the outer edge of the mapped area at ∼220 GHz. As a consequence, there is a decrease in sensitivity at the edges of the map where the SB pseudo-ring is observed. Fortunately, project ID 2011.0.00083.S (∼350 GHz; García-Burillo et al. 2014) is an 11-field mosaic that fully covers the SB pseudo-ring.

For further inspection of the reduced data cubes and spectral line identification and analysis, we have used MADCUBA[1] (Martín et al. 2019). Order 0–1 polynomial baselines were subtracted from the extracted spectra in the regions of interest. This guarantees a flat spectral baseline in order to carry out the molecular line analysis.

[1]Madrid Data Cube Analysis (MADCUBA) is a software developed in the Center of Astrobiology (Madrid) to visualize and analyse data cubes and single spectra (https://cab.inta-csic.es/madcuba/).

Downloaded from https://academic.oup.com/mnras/article/502/2/3021/6119921 by guest on 11 February 2026

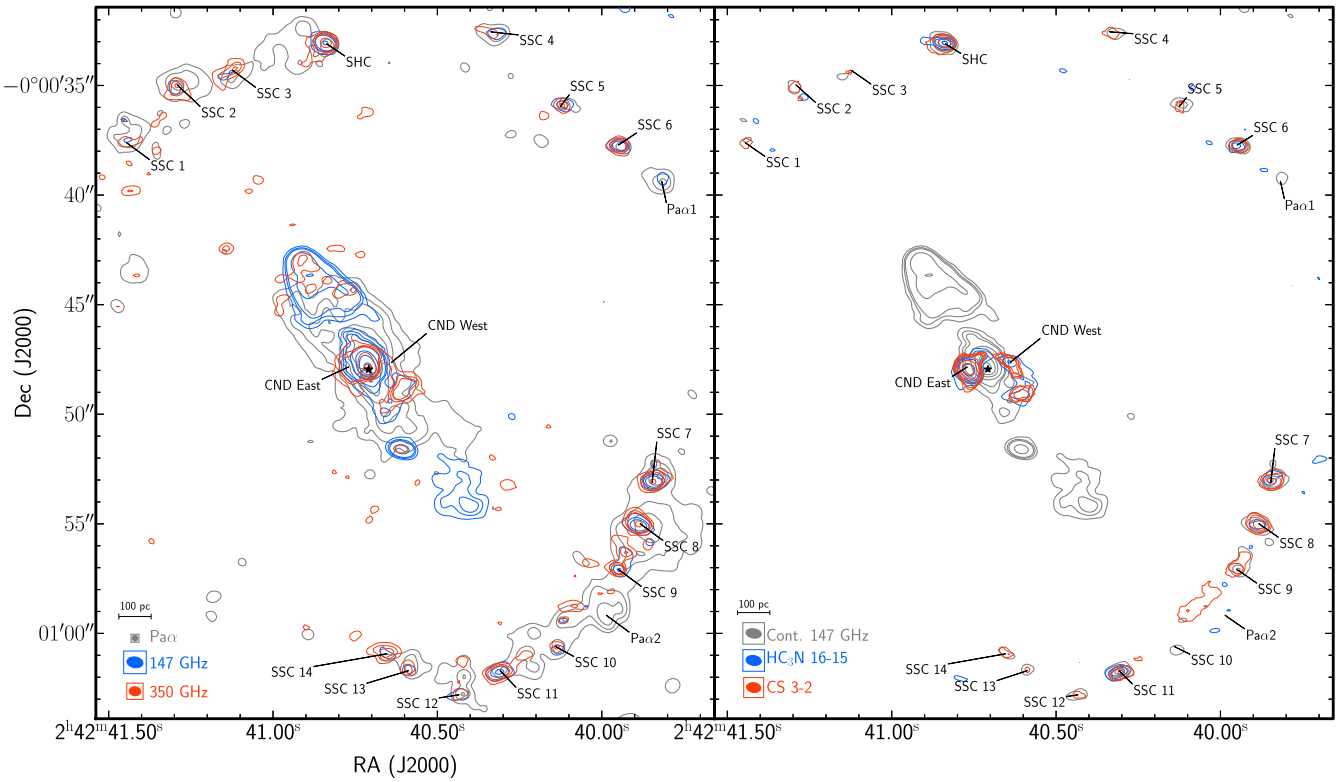


Figure 1. Left-hand panel: (sub)millimetre continuum and Pa α emission map of NGC 1068. The continuum map at 147 GHz is shown in blue, with contour levels of 5 $\times$ σ_{147}, 10 $\times$ σ_{147}, 15 $\times$ σ_{147}, 50 $\times$ σ_{147}, 150 $\times$ σ_{147}, 300 $\times$ σ_{147}, and 600 $\times$ σ_{147}, with $\sigma_{147} = 0.025$ mJy per beam. The continuum map at 350 GHz is shown in red with contour levels of 5 $\times$ σ_{350}, 10 $\times$ σ_{350}, 15 $\times$ σ_{350}, 50 $\times$ σ_{350}, and 150 $\times$ σ_{350}, with $\sigma_{350} = 0.10$ mJy per beam. Pa α emission is shown in grey with contour levels of 10 $\times$ $\sigma_{\mathrm{Pa}\alpha}$, 20 $\times$ $\sigma_{\mathrm{Pa}\alpha}$, 40 $\times$ $\sigma_{\mathrm{Pa}\alpha}$, 80 $\times$ $\sigma_{\mathrm{Pa}\alpha}$, 160 $\times$ $\sigma_{\mathrm{Pa}\alpha}$, and 320 $\times$ $\sigma_{\mathrm{Pa}\alpha}$, with $\sigma_{\mathrm{Pa}\alpha} = 2 \times 10^{-16}$ erg cm^{-2} s^{-1}. Right-hand panel: integrated intensity map of HC_3N $v = 0$ (16–15) (in blue) and CS (3–2) (in red) line emission over the 147 GHz continuum map (in grey). The star marks the AGN position. Indicated are also the 14 continuum clumps identified on the SB pseudo-ring, the SHC position, the two positions with Pa α emission but no 350 GHz continuum, and the two CND positions studied. The beams of each map are shown on the lower left corner of each panel.

Table 1. ALMA observations used in this work.

Project ID	Frequency (GHz)	Resolution (arcsec^2)	rms (mJy per beam)	FOV (arcsec)
2013.1.00055.S	85.37–100.99	0.73 × 0.46	0.67	62.49
2013.1.00221.S	85.55–98.54	0.72 × 0.46	0.37	63.26
2013.1.00279.S	88.61–104.30	0.67 × 0.43	0.54	60.37
2013.1.00279.S	92.54–108.24	0.60 × 0.38	0.96	58.00
2013.1.00060.S	96.25–110.05	1.15 × 0.99	0.62	56.45
2013.1.00221.S	128.83–130.71	0.45 × 0.35	0.37	44.87
2015.1.01144.S	143.62–159.44	0.65 × 0.44	0.62	38.43
2016.1.00232.S	215.35–231.97	0.33 × 0.26	0.43	26.04
2011.0.00083.S	342.27–357.92	0.42 × 0.55	3.48	48.69[a]
2016.1.00232.S	343.56–358.29	0.22 × 0.19	0.77	16.59

[a]Mosaic.

3 RESULTS

3.1 Pa α and continuum emission

The left-hand panel of Fig. 1 shows the ALMA continuum emission maps obtained at 147 GHz and at 350 GHz overlaid on the Pa α emission. The figure also labels the main identified features in NGC 1068 discussed in this paper. As expected, the Pa α emission shows a spatial distribution different from the mm–submm continuum emission. This is partially due to the extinction of the Pa α lines by dust, and also because it traces a less embedded and more evolved stage in the process of massive SF in the SB pseudo-ring (Sánchez-García et al., in preparation).

From the continuum maps at 147 and 350 GHz, we have identified 15 clumps above 5σ in the SB pseudo-ring. We have named these positions SSCs because they have stellar masses of $\sim 10^5$ $M_\odot$ (Section 4.1). In addition, we have detected HC_3N^* emission in one of these SSCs, which we named SHC (Section 3.2).

We have also selected two representative sources that are bright in Pa α (Pa α 1 and Pa α 2) but do not have any associated 350 GHz emission. In addition, we have also included two CND positions, located east and west from the AGN. Their coordinates are listed in Table 2.

To perform the analysis of the continuum emission, we have smoothed the Pa α and 350 GHz images to the same spatial resolution of the 147 GHz map (i.e. 0.62 arcsec $\times$ 0.42 arcsec). We have then measured the peak continuum emission in the three maps at the location of the 147 GHz maximum (see Table 3).

The continuum emission at 147 GHz in the CND is mainly dominated by the non-thermal synchrotron emission from the AGN and the bipolar radio jets interacting with the ISM and its AGN-driven outflow (García-Burillo et al. 2014). In the SB pseudo-ring, the continuum emission at 147 GHz is expected to be mainly dominated by free–free emission. The flux at 8.4 GHz measured with the Very Large Array with an angular resolution of 3.5 arcsec $\times$ 2.9 arcsec at the SHC is $\sim$1.6 Jy (Anantharamaiah et al. 1993), which is consistent with optically thin free–free emission at 147 GHz as the spectral index between these frequencies is ~ -0.1. However, the beam sizes are rather different. We can also use the continuum emission at

Downloaded from https://academic.oup.com/mnras/article/502/2/3021/6119921 by guest on 11 February 2026

Table 2. Coordinates and velocities of the analysed clumps.

Location	RA (J2000) $02^h\,42^m$	Dec. (J2000) -00°	V_{LSR} (km s^{-1})
SHC	40.s84	00′ 32.″94	1094.3 ± 0.3
SSC 1[a]	41.s44	00′ 37.″48	1004.4 ± 1.2
SSC 2[a]	41.s29	00′ 34.″97	1054.8 ± 1.1
SSC 3[a]	41.s15	00′ 34.″64	1067.0 ± 2.3
SSC 4[a]	40.s32	00′ 32.″66	1168.0 ± 0.9
SSC 5[a]	40.s12	00′ 35.″87	1174.1 ± 1.1
SSC 6	39.s95	00′ 37.″75	1193.2 ± 0.6
SSC 7	39.s84	00′ 53.″12	1287.1 ± 0.3
SSC 8	39.s88	00′ 54.″96	1277.3 ± 0.4
SSC 9	39.s95	00′ 57.″88	1263.5 ± 0.3
SSC 10[a]	40.s13	01′ 00.″76	1250.2 ± 1.0
SSC 11	40.s30	01′ 01.″64	1193.0 ± 0.5
SSC 12[a]	40.s44	01′ 02.″85	1143.9 ± 0.7
SSC 13[a]	40.s59	01′ 01.″61	1135.1 ± 1.6
SSC 14[a]	40.s65	01′ 00.″95	1126.4 ± 1.5
Paα 1[a]	39.s81	00′ 39.″37	1205.8 ± 0.8
Paα 2[a]	39.s97	00′ 59.″28	1247.3 ± 0.9
CND E.	40.s77	00′ 47.″84	1076.3 ± 0.6
CND W.	40.s64	00′ 47.″64	1191.8 ± 1.1

[a]Velocity derived from CS since no HC_3N was detected.

Table 3. Peak flux densities of the Paα and 147/350 GHz continuum emission measured towards the position of the 147 GHz continuum peak for each source. The three emission maps have been smoothed to a common resolution of 0.62 arcsec × 0.42 arcsec in order to measure the fluxes. Paα is measured in 10^{-14} erg cm^{-2} s^{-1}, while Cont. 147 and Cont. 350 in mJy per beam. θ^2_{350}, in arcsec^2 (1 arcsec ∼ 70 pc), is the deconvolved surface area obtained from fitting a two-dimensional Gaussian to the 350 GHz continuum emission.

Location	Paα	Cont. 147	Cont. 350	θ^2_{350}
SHC	1.42 ± 0.01	1.37 ± 0.03	7.54 ± 0.12	0.26 ± 0.04
SSC 1	1.96 ± 0.02	0.14 ± 0.02	0.65 ± 0.12	0.54 ± 0.31
SSC 2	3.17 ± 0.02	0.21 ± 0.02	1.46 ± 0.12	0.72 ± 0.26
SSC 3	0.83 ± 0.02	0.16 ± 0.02	1.20 ± 0.12	1.03 ± 0.22
SSC 4	1.93 ± 0.02	0.25 ± 0.03	0.65 ± 0.09	0.77 ± 0.28
SSC 5	0.71 ± 0.03	0.35 ± 0.03	1.47 ± 0.09	0.23 ± 0.08
SSC 6	0.71 ± 0.02	0.72 ± 0.03	3.18 ± 0.09	0.26 ± 0.04
SSC 7	3.50 ± 0.02	0.76 ± 0.03	5.34 ± 0.12	0.36 ± 0.05
SSC 8	3.31 ± 0.02	0.72 ± 0.03	5.78 ± 0.13	0.45 ± 0.18
SSC 9	1.03 ± 0.02	0.39 ± 0.03	2.51 ± 0.10	0.16 ± 0.09
SSC 10	1.60 ± 0.01	0.25 ± 0.03	0.91 ± 0.11	0.23 ± 0.10
SSC 11	1.21 ± 0.01	0.42 ± 0.03	3.28 ± 0.11	0.50 ± 0.12
SSC 12	1.27 ± 0.01	0.21 ± 0.03	0.67 ± 0.11	0.57 ± 0.20
SSC 13	1.71 ± 0.02	0.19 ± 0.03	1.22 ± 0.11	0.33 ± 0.10
SSC 14	0.64 ± 0.02	0.18 ± 0.03	1.94 ± 0.11	0.79 ± 0.13
Paα 1	2.19 ± 0.03	0.18 ± 0.04	≤0.26	0.43 ± 0.38
Paα 2	1.37 ± 0.02	≤0.13	≤0.35	0.29 ± 0.27
CND E.	6.57 ± 0.01	0.65 ± 0.01	3.72 ± 0.08	–
CND W.	5.31 ± 0.03	0.12 ± 0.01	0.51 ± 0.08	–

350 GHz to estimate the possible contribution from dust emission to the 147 GHz continuum emission. Assuming that the dust emission measured at 350 GHz is optically thin and a typical dust emissivity spectral index of 1.5, the expected contribution of the dust emission to the 147 GHz flux will be only of about 20 per cent; i.e. the 147 GHz continuum is dominated by the free–free emission. In the following discussion, we will consider that the continuum emission at 350 GHz is dominated by dust emission both towards the CND and the SB pseudo-ring. Both continuum emissions coincide spatially on the SB pseudo-ring, where they exhibit a clumpy structure associated with star-forming regions. Note that non-thermal emission dominates throughout the radio jet trajectory (which encloses the CND east knot; for a detailed analysis on the CND spectral indexes, see García-Burillo et al. 2019).

3.2 HC_3N emission

The right-hand panel of Fig. 1 shows the distribution of the HC_3N $v = 0$ ($J = 16$–15) and the CS ($J = 3$–2) velocity-integrated line emission overlaid on the 147 GHz continuum emission. This figure shows that the HC_3N $v = 0$ ($J = 16$–15) and CS ($J = 3$–2) lines trace the CND and the high-density SF clumps in the SB pseudo-ring and closely follows the 147 GHz continuum in those regions. HC_3N emission is detected in sources with radio continuum and/or Paα emission, namely positions CND E., CND W., SHC, and SSC 6, 7, 8, 9, and 11. We have measured the velocity of the gas for the positions in Table 2 from HC_3N $v = 0$ emission (when detected) and from CS. Other molecules such as CO, HCN, HNCO, H_2CO, or CH_3OH were also detected, but in this paper we will focus on the HC_3N emission of the selected positions.

In addition to the HC_3N emission from the ground vibrational state, we have searched for HC_3N^* emission from the SB pseudo-ring and the CND. Table 4 lists the spectroscopic parameters of the HC_3N^* transitions observed in our data. We have detected HC_3N^* emission from the $v_7 = 1$ vibrationally excited state in the rotational transitions $J = 16$–15 ($E_u = 380$ K) and $J = 24$–23 ($E_u = 452$ K) towards only one condensation in the SB pseudo-ring, hereafter the SHC. Integrated intensities in the SHC of rotational transitions from the $v_6 = 1$ vibrationally excited state are just below 1σ and we treat them as undetected. Fig. 2 displays the spectra of HC_3N from the rotational transitions $J = 16$–15, 24–23, and 39–38 in the ground, $v_7 = 1$, and $v_6 = 1$ vibrational states towards the SHC. The lack of sensitivity prevented us from detecting HC_3N^* emission towards any other position in the SB pseudo-ring. It is remarkable that, in spite of the enhanced column density of HC_3N in the CND (see Section 4.2), we have not detected any HC_3N^* emission towards the CND positions. Like Fig. 2, Fig. 3 shows the spectra of the rotational transitions in the $v = 0$ and $v_7 = 1$ vibrational states towards CND east. The integrated fluxes for the observed HC_3N^* transitions for the most relevant positions (SHC, SSC 7, CND east, and CND west) are listed in Table 5, with non-detected lines represented as upper limits with their corresponding 3σ integrated intensity values. It is worth noting the large contrast between the $v = 0$ and $v_7 = 1$ rotational lines.

4 ANALYSIS

4.1 Stellar and gas masses in the SB pseudo-ring

We can use the Paα and the continuum emission at 147 GHz dominated by free–free emission to estimate the stellar mass of massive stars that just joined the main sequence (i.e. zero age main sequence stars; ZAMS). Using the canonical values for an H II region of $T_e = 10^4$ K and electron density $n_e = 10^4$ cm^{-3}, the production rate of ionizing photons from the Paα peak emission, $Q^0_{L_{Pa\alpha}}$, is (Kennicutt 1998; Osterbrock & Ferland 2006)

$$Q^0_{L_{Pa\alpha}}(s^{-1}) = 7.344 \times 10^{12} \left(\frac{L_{Pa\alpha}}{\text{erg s}^{-1}}\right) \quad (1)$$

Downloaded from https://academic.oup.com/mnras/article/502/2/3021/6119921 by guest on 11 February 2026

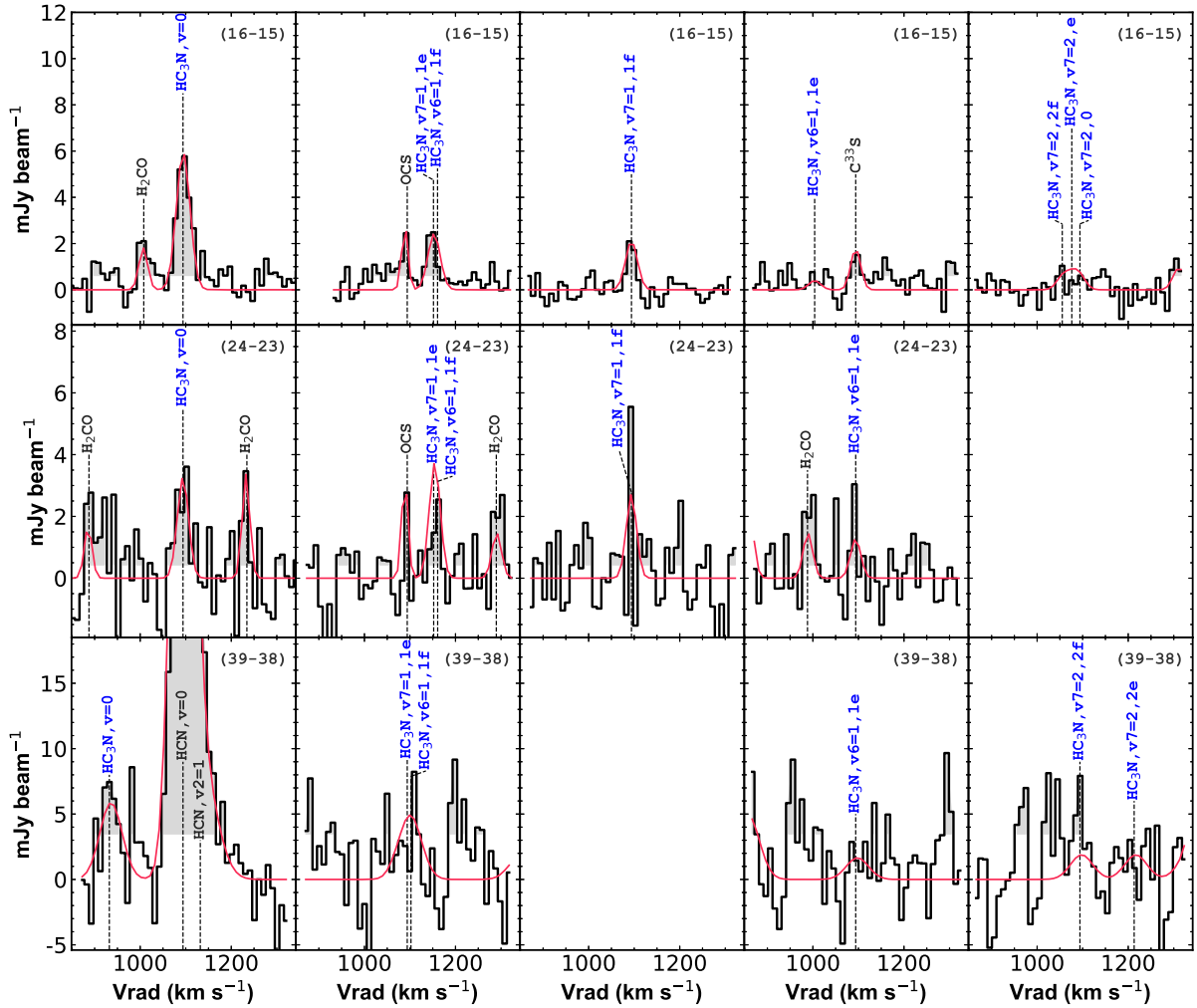


Figure 2. Observed spectra (black histograms) towards the SHC. HC_3N^* lines are highlighted in blue. Grey shaded spectra represent values above the 1σ level. Each row corresponds to a different (J_{up}–J_{low}) transition (indicated on the top-right corner of each panel), The top row corresponds to $J = 16$–15, the middle row to $J = 24$–23, and the bottom row to $J = 39$–38. HC_3N transitions from the same vibrational state and wavefunction parity but different (J_{up}–J_{low}) are organized in columns. Empty panels reflect that there are no data available for that HC_3N transition (i.e. the $J = 39$–38 HC_3N, $v_7 = 1$, 1f and all $J = 24$–23 HC_3N, $v_7 = 2$ transitions). The red lines represent the fitted LTE model obtained from MADCUBA.

The values can change ∼15 per cent due to variations in the electron temperature within $T_e = 5000$–$20\,000$ K and remain insensitive for electron density variations within $n_e = 10^2$–10^6 cm^{-3} (Osterbrock & Ferland 2006; Piqueras López et al. 2016). We can also obtain the production rate of ionizing photons from the continuum emission at 147 GHz, Q^0_{147}, using the approach by Murphy et al. (2011) and assuming the same T_e as for the determination of the $Q^0_{L_{Pa\alpha}}$:

$$Q^0_{147}(\mathrm{s}^{-1}) = 10^{26} \left(\frac{T_e}{10^4\,\mathrm{K}}\right)^{-0.45} \left(\frac{\nu}{147\,\mathrm{GHz}}\right)^{0.1} \left(\frac{L_{147}}{\mathrm{erg\ s^{-1}\ Hz^{-1}}}\right). \quad (2)$$

Finally, we convert the ionizing photons production rates to ZAMS stellar masses (M_*) following Leroy et al. (2018):

$$M_*(\mathrm{M}_\odot) \sim \frac{Q^0}{4 \times 10^{46}}. \quad (3)$$

The ZAMS stellar masses derived from the ionizing photons production rates from Pa α and 147 GHz continuum emission ($M_{*,Pa\alpha}$ and $M_{*,147}$) are compared in Table 7. The mass of ZAMS stars in all condensations with radio continuum emission is a few 10^5 M$_\odot$, typical of the SSCs (young star clusters with stellar masses $\gtrsim 10^4$ M$_\odot$) found in NGC 253 (Rico-Villas et al. 2020), indicating that a substantial fraction of the SF in the SB pseudo-ring seems to be dominated by SSCs.

On the other hand, we can use the 350 GHz continuum emission to estimate the total gas mass from dust emission. Following Leroy et al. (2018), we first estimate the optical depth (τ_{350}) by comparing the measured intensity peak (I_{350}) with that expected by assuming a dust temperature:

$$I_{350} = (1 - \mathrm{e}^{\tau_{350}})\, B_\nu(T_{dust}), \quad (4)$$

where B_ν is the blackbody intensity at 350 GHz for a given dust temperature. For our mass estimates, we have assumed a dust temperature of 80 K (see Leroy et al. 2018, for SSCs in NGC 253). Changes in a factor of 2 in T_{dust} will change the masses by a similar factor. Assuming a mass absorption coefficient of $\kappa_{350} = 1.9\,\mathrm{cm^2\ g^{-1}}$ (Leroy et al. 2018) and a standard dust-to-gas ratio (DGR) of 1/100 by mass [close to the value found by Wilson et al. (2008) for SB galaxies and similar to the 1/150 value commonly used for the MW], we can convert τ_{350} into a gas surface density (Σ_{gas}) that is then

Downloaded from https://academic.oup.com/mnras/article/502/2/3021/6119921 by guest on 11 February 2026

Table 4. HC_3N^* transition quantum numbers and frequencies present in the analysed data.

Vib. state	J_{up}–J_{low}	l-doubling ($l_{up} - l_{low}$)	Parity	Frequency (GHz)	E_{up} (K)	g_{up}
$v = 0$	10–9	–	–	90.98	24	21
$v = 0$	11–10	–	–	100.08	29	23
$v = 0$	12–11	–	–	109.17	34	25
$v = 0$	16–15	–	–	145.56	59	33
$v_6 = 1$	16–15	(−1, +1)	1e	145.80	777	33
$v_6 = 1$	16–15	(+1, −1)	1f	145.91	777	33
$v_7 = 1$	16–15	(−1, +1)	1e	145.92	380	33
$v_7 = 1$	16–15	(+1, −1)	1f	146.13	380	33
$v_7 = 2$	16–15	(0, 0)	0	146.48	701	33
$v_7 = 2$	16–15	(−2, +2)	2e	146.48	705	33
$v_7 = 2$	16–15	(+2, −2)	2f	146.49	705	33
$v = 0$	24–23	–	–	218.32	131	49
$v_6 = 1$	24–23	(−1, +1)	1e	218.68	849	49
$v_6 = 1$	24–23	(+1, −1)	1f	218.85	849	49
$v_7 = 1$	24–23	(−1, +1)	1e	218.86	452	49
$v_7 = 1$	24–23	(+1, −1)	1f	219.17	452	49
$v_7 = 2$	24–23	(0, 0)	0	219.68	774	49
$v_7 = 2$	24–23	(−2, +2)	2e	219.71	777	49
$v_7 = 2$	24–23	(+2, −2)	2f	219.74	777	49
$v = 0$	38–37	–	–	345.61	324	77
$v = 0$	39–38	–	–	354.70	341	79
$v_6 = 1$	39–38	(+1, −1)	1e	355.28	1059	79
$v_6 = 1$	39–38	(−1, +1)	1f	355.56	1059	79
$v_7 = 1$	39–38	(+1, −1)	1e	355.57	662	79
$v_7 = 1$	39–38	(−1, +1)	1f	356.07	663	79
$v_7 = 2$	39–38	(+2, −2)	2e	356.94	988	79
$v_7 = 2$	39–38	(−2, +2)	2f	357.08	988	79

converted into gas mass from the cloud surface area (θ^2):

$$M_{gas}(M_\odot) = \theta^2 \Sigma_{gas} = \theta^2 \frac{1}{DGR \times \kappa_{350}} \tau_{350}. \quad (5)$$

The cloud surface areas have been derived from a two-dimensional Gaussian fitting to the 350 GHz continuum emission after deconvolution of the beam profile. The values of θ^2 are listed in Table 3 and the gas masses in Table 7.

4.2 Physical properties derived from HC_3N

Following the procedure used for NGC 253 in Rico-Villas et al. (2020), we have used both local thermodynamic equilibrium (LTE) and non-LTE multiline analyses of the HC_3N emission from the $v = 0$ and $v_7 = 1$ vibrational states to derive the physical properties of the star-forming regions in the SB pseudo-ring and the CND. We analyse the HC_3N emission in sources where emission from the $v = 0$ is detected and we also include some positions with no HC_3N emission for completeness (e.g. SSC 2, Pa α 1, and Pa α 2).

The excitation of HC_3N can be dominated by different mechanisms: While its vibrational transitions are pumped mainly via absorption of mid-IR photons (IR pumping), the excitation of the rotational levels within a given vibrational state is usually dominated by collisions with H_2 (Rico-Villas et al. 2020).

4.2.1 LTE analysis

To describe both types of excitations, two different excitation temperatures are used, in LTE the vibrational temperature (T_{vib}) describing the excitation between vibrational levels, and the rotational temperature (T_{rot}) describing the excitation between rotational levels within a vibrationally excited state. Usually, T_{vib} reflects the dust temperature in the case of IR pumping (Rico-Villas et al. 2020).

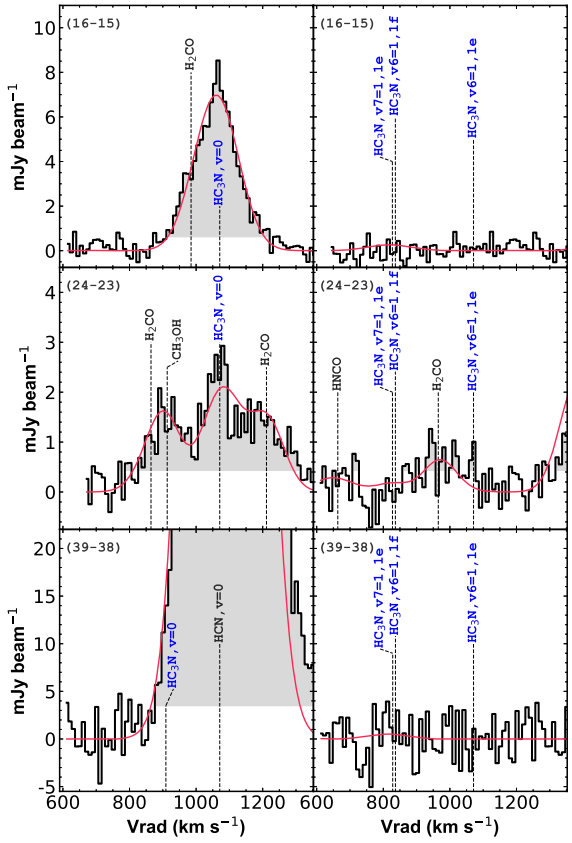


Figure 3. Observed spectra (black histograms) together with the fitted MADCUBA LTE profiles (solid red lines) towards the CND east position. The position of the HC_3N transitions is highlighted in blue and blended lines from other identified molecules are shown with grey labels. Grey shaded areas under the profiles represent intensities above the spectra rms. Each row corresponds to a different (J_{up}–J_{low}) HC_3N transition, shown in the upper left corner of every panel. The left column corresponds to transitions from the $v = 0$ ground state and the right column to the (undetected) transitions from the $v_7 = 1$ and $v_6 = 1$ vibrationally excited states.

The need of two excitation temperatures to describe the excitation of HC_3N is illustrated in the rotational diagram (Fig. 4). The rotational diagram can be used to obtain total column densities and excitation temperatures from line integrated intensities. A detailed explanation on the rotational diagram method can be found in Goldsmith & Langer (1999). In short, assuming that the emission is optically thin, HC_3N column densities from the upper level can be derived as follows:

$$N_u^{thin} = \frac{8\pi k \nu^2 W}{hc^3 A_{ul}}, \quad (6)$$

where W is the integrated line intensity (in K km s^{-1}) and A_{ul} is the Einstein coefficient for spontaneous emission, which, in the case of a linear molecule such as HC_3N, can be obtained from Table 4 using equation (25) from Goldsmith & Langer (1999) and assuming an electric dipole moment of $\mu = 3.73$ D (DeLeon & Muenter 1985). Then, we relate upper level and total column densities by

$$\frac{N_u}{g_u} = \frac{N}{Z} e^{-E_u/kT}, \quad (7)$$

Downloaded from https://academic.oup.com/mnras/article/502/2/3021/6119921 by guest on 11 February 2026

Table 5. MADCUBA-fitted integrated intensity for HC_3N emission lines in mJy beam^{-1} km s^{-1} for the SHC, SSC 7, CND east, and CND west positions. Upper limits are 3σ.

Transition		SHC	SSC 6	SSC 7	SSC 8	SSC 9	SSC 11	CND E	CND W
$v = 0$	10–9	41 ± 10	≤29	27 ± 6	46 ± 12	44 ± 12	≤28	–	–
$v = 0$	11–10	109 ± 27	73 ± 15	79 ± 12	89 ± 14	39 ± 12	50 ± 14	477 ± 119	108 ± 27
$v = 0$	12–11	137 ± 34	60 ± 15	64 ± 16	64 ± 14	56 ± 13	79 ± 15	734 ± 183	308 ± 77
$v = 0$	16–15	224 ± 56	84 ± 11	98 ± 24	73 ± 12	35 ± 12	97 ± 11	1124 ± 281	306 ± 76
$v = 0$	24–23	113 ± 28	≤43	65 ± 16	≤47	≤43	≤46	234 ± 59	≤89
$v = 0$	38–37	381 ± 95	≤184	≤195	≤191	≤172	≤180	≤1769[a]	≤243[a]
$v = 0$	39–38	282 ± 70	≤171	≤181	≤178	≤160	≤168	≤304[b]	≤350[b]
$v_7 = 1$	16–15 1e	59 ± 15	≤32	≤33	≤35	≤31	≤33	≤82	≤86
$v_7 = 1$	16–15 1f	58 ± 15	≤32	≤33	≤35	≤31	≤33	≤82	≤86
$v_7 = 1$	24–23 1e	50 ± 13	≤42	≤46	≤46	≤41	≤44	≤81	≤89
$v_7 = 1$	24–23 1f	50 ± 13	≤42	≤46	≤46	≤41	≤44	≤81	≤89

[a]Strongly blended with CO(3–2) due to the higher FWHMs in the CND (see Table 6).
[b]Blended with HCN(4–3) due to the higher FWHMs in the CND (see Table 6).

where Z is the HC_3N partition function obtained from the CDMS[2] catalogue (Müller et al. 2001, 2005). Rearranging and taking the logarithm on both sides of equation (7), we obtain

$$\log\left(\frac{N_u}{g_u}\right) = \log\left(\frac{N}{Z}\right) - \log(e)\frac{E_u}{kT}, \quad (8)$$

from which we can derive the total column density N and the excitation temperature T by fitting a straight line using the least-squares method.

Fig. 4 upper and lower panels show the rotational diagram for the detected HC_3N^* transitions towards the SHC and CND east condensation. The difference between $T_{\rm rot}$ and $T_{\rm vib}$ is clearly illustrated by the dashed and colour solid lines. By fitting equation (8) to the transitions from the same rotational levels ($J = 16$–15 or 24–23) but different vibrational states, we estimate a vibrational temperature of $T_{\rm vib,16-15} = 239 \pm 30$ K and $T_{\rm vib,24-23} = 390 \pm 122$ K for the SHC. These temperatures are clearly higher than the lower rotational temperature $T_{\rm rot,v=0} = 103 \pm 14$ K, obtained by fitting equation (8) to all the transitions observed from the ground state (Fig. 4). For the CND east, since no HC_3N^* was detected, we derived an upper limit $T_{\rm vib,16-15} \leq 122$ K from the $v_7 = 1$ $J = 16$–15 and a $T_{\rm rot,v=0} = 42 \pm 10$ K. The errors have been obtained from bootstrapping using the uncertainties of the line fluxes. It is remarkable that the gas in the CND surrounding the SMBH seems to have lower excitation temperatures than the gas in the star-forming regions.

To fully account for the line profiles, opacity effects, and line blending, we have also carried out an LTE analysis of the HC_3N^* emission using the MADCUBA SLIM tool (Martín et al. 2019). Figs 2 and 3 show the predicted SLIM line profiles superimposed on the observed spectra for the SHC and CND east, respectively. The fitted parameters with their associated errors are given in Table 6. For the SLIM fitting, we have used a source size of 0.42 arcsec, the smallest beam with HC_3N data that reproduces the observed $v = 0$ lines, although the emitting region of $v_7 = 1$ clearly must be smaller since it must arise from a region with a higher IR photon flux in order to be vibrationally excited. We derive for the SHC $T_{\rm vib} = 236 \pm 16$ K and $T_{\rm rot} = 98 \pm 7$, similar to those derived from the rotational diagram. The derived line optical depths are <0.01, indicating that the optically thin assumption for the rotational diagram method is valid. For the CND positions, where HC_3N^* emission is not detected despite the large HC_3N $v = 0$ column density, we have derived upper limits of $T_{\rm vib} \lesssim 98$ and $\lesssim$117 K for the east and west positions, respectively. The derived $T_{\rm rot}$ from the emission of the $v = 0$ states in the CND is also much lower than that in the SHC, reflecting lower excitation conditions (see below).

From the non-detection of HC_3N^* in other star-forming regions of the SB pseudo-ring, we cannot completely rule out the presence of SHCs, since their upper limits to the emission from the $v_7 = 1$ lines are still consistent with $T_{\rm vib} \sim 150$–226 K as derived from $J = 16$–15 HC_3N $v = 0$ and $v_7 = 1$ lines upper limits. Furthermore, SSC 7 and 8 have $T_{\rm rot,v=0}$ very similar to the SHC, indicating similar physical conditions that are fully consistent with the presence of SHCs, i.e. internally heated. Conversely, SSC 6, 9, and 11 indicate $T_{\rm vib} \lesssim 180$ K and $T_{\rm rot}$ ~20–40 K, which are much lower than those in the SHC, pointing to a lack of SHCs associated with these condensations.

4.2.2 *Non-LTE analysis*

To derive the physical properties of the SHC and the CND and to properly account for the different excitation mechanisms of the vibrational and rotational HC_3N transitions, we have carried out a non-LTE radiative transfer modelling using the same code used in Rico-Villas et al. (2020) (described in detail in González-Alfonso & Cernicharo 1997, 1999; González-Alfonso & Sakamoto 2019), which includes the HC_3N rotational transitions up to $J = 45$ in the $v = 0$, $v_7 = 1$, and $v_6 = 1$ vibrational states. As illustrated in fig. 4 by Rico-Villas et al. (2020), the ratio between the $v_7 = 1$ and $v = 0$ rotational lines from the same rotational level is extremely sensitive to the dust temperature, and the ratio between lines from different rotational levels but from the same vibrational state is dependent on the $n_{\rm H_2}$ density.

For NGC 1068, we consider the ratios of the $v = 0$ and $v_7 = 1$ $J = 24$–23 and $J = 16$–15 lines, since $J = 39$–38 are undetected except for the SHC position. Using the ratio between the $J = 16$–15 rotational transitions from the $v = 0$ and $v_7 = 1$ states (v_0/v_7), we find for the SHC a dust temperature of $T_{\rm d} = 248 \pm 28$ K, very close to the previously derived $T_{\rm vib} = 236 \pm 18$, and a density of $n_{\rm H_2} = (5.9 \pm 0.2) \times 10^5$ cm^{-3}.

For the other positions, since no $v_7 = 1$ line is detected, we only have a lower limit on the ratio v_0/v_7 and we assume $T_{\rm vib}$ derived from LTE as their dust/kinetic temperature upper limit. To better constrain the dust temperatures and since the model also returns the spectral energy distribution (SED), we also fit the observed continuum emission at 350 GHz. The obtained dust temperatures are similar to $T_{\rm vib}$ derived from the LTE modelling.

[2]http://www.astro.uni-koeln.de/cgi-bin/cdmssearch

Downloaded from https://academic.oup.com/mnras/article/502/2/3021/6119921 by guest on 11 February 2026

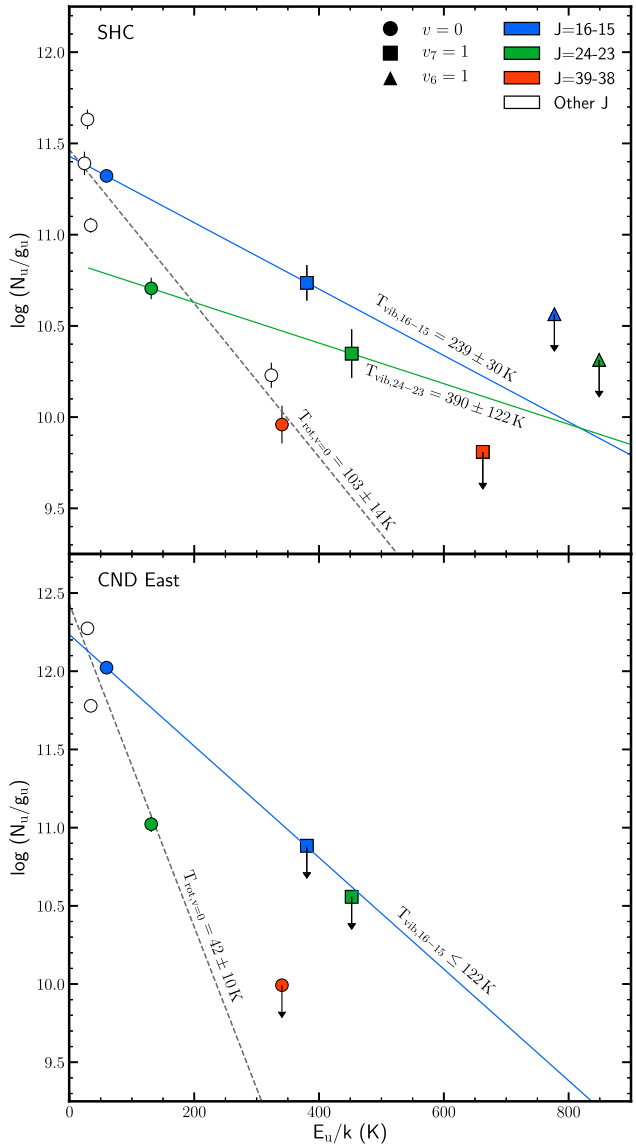


Figure 4. Rotational diagram derived from the line intensities of HC_3N^* for the SHC position (upper panel) and CND east position (lower panel). Transitions from the ground state $v = 0$ are marked with circles, $v_7 = 1$ with squares, and $v_6 = 1$ with triangles. The $J = 39$–38 transitions are highlighted in red, $J = 24$–23 in green, and $J = 16$–15 in blue. Dashed grey lines represent the fit to all rotational transitions (J_{up}–J_{low}) from the ground state $v = 0$ (i.e. $T_{rot,v=0}$). The blue and green solid line represents the fit to the $J = 16$–15 and 24–23 transitions from the $v = 0$ and $v_7 = 1$ states, respectively (i.e. $T_{vib,16-15}$ and $T_{vib,24-23}$). Errors have been obtained from bootstrapping.

In particular, for the CND east position, the derived parameters from the models are $T_d \leq 75$ K, a density $n_{H_2} = (5.9 \pm 0.3) \times 10^5$ cm^{-3}, and an HC_3N column density of $N_{HC3N} = (9.5 \pm 2.9) \times 10^{15}$ cm^{-2} with a fractional abundance of $X_{HC3N} = (3.7 \pm 1.1) \times 10^{-9}$ (Table 6). It is worth noting that the dust temperatures towards the CND east and west positions are much lower than that derived for the SHC, despite the other parameters remaining similar to the SHC. The parameters for the CND are in agreement with those estimated by Viti et al. (2014), who derived densities for the CND of (5–10) $\times 10^5$ cm^{-3} and a kinetic temperature of 60 and 100–150 K for the CND east and west positions, respectively. González-Alfonso et al. (2014), from modelling of the H_2O submillimetre emission, found $T_d \sim 55$ K and high densities of $n(H_2) \sim 10^6$ cm^{-3}, similar to the values we obtained.

4.2.3 *Proto-SSC in the SB pseudo-ring: mass and luminosity*

The physical conditions of the SHC (and also SSC 7 and 8) in NGC 1068, high T_{vib} and H_2 densities of few 10^5 cm^{-3}, are similar to those found in the SHCs of NGC 253, where the IR emission from the dust heated by massive protostars vibrationally excites HC_3N. Rico-Villas et al. (2020) proposed that the SHCs trace the earliest phase of SSCs formation, the proto-SSC phase. Following the analysis presented in Rico-Villas et al. (2020), we have estimated the LTE and non-LTE luminosities of the condensations (clumps) studied in this work. For the LTE luminosities, we have used the emission of a blackbody with a (dust) temperature of T_{vib} and the lower limit to the size of the SHC of 0.021 arcsec (1.41 pc) derived by assuming that the emission from the $v_7 = 1$ HC_3N $J = 16$–15 line is optically thick (i.e. the source brightness temperature is equal to the derived vibrational/dust temperature; see Rico-Villas et al. 2020). The same size is used to derive the upper limits for the other sources without detected HC_3N^* emission. The non-LTE luminosity is derived from the SED between 10 and 1200 μm predicted from the non-LTE models and assuming the same lower limit size as for the LTE estimate.

These estimates need to be corrected by the back warming/greenhouse effect (Donnison & Williams 1976; González-Alfonso & Sakamoto 2019), which appears in IR optically thick condensations when a fraction of the IR radiation returns to the source (back warming), achieving the thermal equilibrium at a higher dust temperature than expected for the optically thin case. For the $N_{H_2} \sim 10^{24}$ cm^{-2} derived for the SHC, the apparent luminosities need to be corrected by a factor of 0.2 (Rico-Villas et al. 2020); i.e. the actual luminosities will be 5 times smaller than the directly estimated from the analysis, obtaining for the SHC 5.8×10^8 and 5.9×10^8 $L_\odot$ from the LTE and non-LTE models, respectively. The luminosities corrected from back warming for all sources are listed in Table 6.

From these luminosities, we can make an estimate of the mass in protostars (M_{p*}) by assuming a luminosity-to-mass ratio of 10^3 $L_\odot$ $M_\odot^{-1}$ (similar to the luminosity-to-mass ratio typically assumed for ZAMS stars since the time-scales for massive protostars to reach the ZAMS are short and expected to follow the ZAMS evolutionary track; Hosokawa & Omukai 2009; Rico-Villas et al. 2020). The protostar masses of the SSCs in NGC 1068 are given in Table 7. The luminosity and mass of protostars in the SSCs of NGC 1068 are similar to those found in NGC 253. The non-detection of HC_3N^* emission in the remaining SSCs prevents us from firmly establishing to what extent they are still undergoing the proto-SSC phase (see below), apart from the SHC clump.

5 DISCUSSION

5.1 On the heating of the SHC and the CND

As already mentioned, the excitation of HC_3N can be dominated by two different mechanisms: IR radiation pumping by hot dust and/or collisions with H_2, which can be used to discriminate between different heating mechanisms. We have found a significant difference between the derived T_{vib} for the CND east and west positions ($\lesssim$100 K) and for the SHC ($\simeq$240 K). The same trend is also found for the rotational temperature: $T_{rot} = 41$ K for the CND east, 29 K

Downloaded from https://academic.oup.com/mnras/article/502/2/3021/6119921 by guest on 11 February 2026

Table 6. Parameters derived from LTE and non-LTE modelling. LTE HC_3N column densities, rotational temperatures from the ground state (T_{rot}), and vibrational temperatures from HC_3N^* $J = 16$–15 (T_{vib}) were obtained with SLIM assuming a source size of 0.42 arcsec. Positions marked with * have no HC_3N $v = 0$ detected, their FWHMs have been obtained from CS, and a fiducial $T_{rot} = 20$ K and $T_{vib} = 100$ K were assumed in order to derive an upper limit for their HC_3N column densities. All non-LTE parameters are derived for a source size lower limit of 0.02 arcsec.

		LTE				Non-LTE					
Source	FWHM ($km\,s^{-1}$)	log $N(HC_3N)$[a] (cm^{-2})	T_{rot} (K)	T_{vib} (K)	L^{b}_{LTE} ($10^8\,L_\odot$)	n_{H_2} ($10^5\,cm^{-3}$)	log $N(H_2)$[c] (cm^{-2})	log $N(HC_3N)$[c] (cm^{-2})	$X(HC_3N)$ (10^{-9})	T_d (K)	$L^{d}_{n\text{-}LTE}$ ($10^8\,L_\odot$)
SHC	33 ± 2	14.7(13.6)	98 ± 7	236 ± 18	5.8 ± 1.7	5.9 ± 0.2	24.4(23.3)	15.9(15.3)	3.4 ± 0.8	248 ± 28	5.9 ± 2.1
SSC 2*	32	≤13.2	20*	100*	≤0.2	–	–	–	–	–	–
SSC 6	31 ± 4	14.0(12.9)	39 ± 9	≤150	≤1.2	3.0 ± 0.1	24.1(23.4)	16.0(15.6)	7.5 ± 3.3	≤125	≤0.4
SSC 7	27 ± 4	14.1(13.0)	83 ± 16	≤213	≤3.8	3.1 ± 0.6	24.1(23.4)	15.7(15.1)	3.8 ± 1.2	≤190	≤2.4
SSC 8	26 ± 7	14.0(13.0)	72 ± 11	≤226	≤4.8	5.9 ± 0.1	24.4(23.3)	15.7(15.1)	1.9 ± 0.0	≤188	≤2.3
SSC 9	31 ± 2	13.7(13.2)	24 ± 8	≤178	≤0.7	1.5 ± 1.0	23.8(23.5)	15.7(15.3)	8.1 ± 6.1	≤163	≤1.3
SSC 11	34 ± 4	14.0(13.1)	36 ± 7	≤189	≤2.4	3.0 ± 0.1	24.1(23.7)	16.0(15.6)	7.1 ± 3.2	≤181	≤2.1
Pa α 1*	31	≤13.3	20	100	≤0.2	–	–	–	–	–	–
Pa α 2*	30	≤13.4	20	100	≤0.2	–	–	–	–	–	–
CND E.	144 ± 3	15.0(13.3)	41 ± 1	≤98	≤0.2	5.9 ± 0.3	24.4(23.3)	16.0(15.5)	3.7 ± 1.1	≤75	≤0.1
CND W.	149 ± 8	14.4(13.2)	29 ± 3	≤117	≤0.3	3.5 ± 0.5	24.2(23.6)	15.7(14.8)	3.0 ± 0.6	≤114	≤0.1

[a]Column density derived from SLIM assuming a source size of 0.42 arcsec ($r = 14.25$ pc).
[b]Luminosities obtained by assuming a blackbody emitting at T_{vib} and corrected from the back warming effect (see Section 4.2.3).
[c]Column density derived from the non-LTE models assuming a source size lower limit of 0.02 arcsec ($r = 0.71$ pc).
[d]Luminosities obtained from the non-LTE modelled SED between 10 and 1200 μm and corrected from the back warming effect.

Table 7. Summary table with all masses derived. The $M_{*,Pa\alpha}$ and $M_{*,147}$ are the ZAMS stellar masses derived from the Pa α and the 147 GHz continuum emission, respectively. M_{gas} are the gas masses derived from the dust continuum emission at 350 GHz assuming the sizes obtained by fitting a two-dimensional Gaussian to each location, θ^2_{350} in Table 3. $M_{p*,LTE}$ and $M_{p*,nLTE}$ are the proto stellar masses derived from the LTE and non-LTE modelling of HC_3N^* and $t_{age,p*}$ and $t_{age,Pa}$ are the SSC estimated ages following equations (10) and (11). SFE is the star formation efficiency.

Source	$M_{*,Pa\alpha}$ ($10^5\,M_\odot$)	$M_{*,147}$ ($10^5\,M_\odot$)	M_{gas} ($10^5\,M_\odot$)	$M_{p*,LTE}$ ($10^5\,M_\odot$)	$M_{p*,nLTE}$ ($10^5\,M_\odot$)	$M_{*,147}/M_{*,Pa\alpha}$	$M_{p*}/M_{*,147}$	$t_{age,Pa}$ (10^5 yr)	$t_{age,p*}$ (10^5 yr)	SFE
SHC	0.6	7.9	33.2	5.8 ± 1.7	5.9 ± 2.1	13.0	0.7	0.6	0.6	0.2
SSC 1	0.8	0.8	0.7	–	–	1.0	–	≥100	–	0.5
SSC 2	1.4	1.2	3.8	≤0.2	≤0.2	0.9	≤0.2	≥100	≥0.9	0.2
SSC 3	0.4	0.9	1.0	–	–	2.6	–	4.5	–	0.5
SSC 4	0.8	1.4	2.8	–	–	1.7	–	9.7	–	0.3
SSC 5	0.3	2.0	8.2	–	–	6.6	–	1.3	–	0.2
SSC 6	0.3	4.1	9.3	≤1.2	≤0.4	13.5	≤0.3	0.6	≥0.8	0.3
SSC 7	1.5	4.4	10.5	≤3.8	≤2.4	2.9	≤0.7	3.8	≥0.5	0.3
SSC 8	1.4	4.2	18.0	≤4.8	≤2.3	2.9	≤1.2	3.8	≥0.5	0.2
SSC 9	0.4	2.3	15.2	≤0.7	≤1.3	5.1	≤0.3	1.8	≥0.8	0.1
SSC 10	0.7	1.4	3.0	–	–	2.1	–	6.8	–	0.3
SSC 11	0.5	2.4	4.0	≤2.4	≤2.1	4.7	≤0.2	2.0	≥0.5	0.4
SSC 12	0.5	1.2	1.9	–	–	2.3	–	5.8	–	0.4
SSC 13	0.7	1.1	3.1	–	–	1.5	–	12.9	–	0.3
SSC 14	0.3	1.0	5.0	–	–	3.7	–	2.7	–	0.2
Pa α 1	0.9	1.0	≤0.5	≤0.2	–	1.1	≤0.2	40.6	≥0.8	0.7
Pa α 2	0.6	≤0.8	≤0.2	≤0.2	–	≤1.3	≤0.2	≥21.2	≥0.8	0.8

for CND west, and 98 K for the SHC, with SSCs 7 and 8 also having high $T_{rot} \sim 80$ K. The derived H_2 densities for both the SHC and the CND positions are similar, but much lower than the critical density for collisional excitation of the vibrational levels ($>10^8\,cm^{-3}$; Wyrowski et al. 1999). Therefore, the excitation of the vibrational states must be through IR pumping by the hot dust and the excitation of the rotational levels by collisions with H_2.

The CND, located at ∼60–80 pc from the SMBH in NGC 1068, seems to be strongly affected by the interaction with the AGN. Both radiative and mechanical effects have substantially changed its kinematics and physical and chemical properties (Tacconi et al. 1994; Usero et al. 2004; García-Burillo et al. 2010). X-rays from the AGN have been proposed to explain the specific chemistry found in the CND (e.g. Sternberg, Genzel & Tacconi 1994; Usero et al. 2004; Aladro et al. 2012, 2013). Several studies have analysed the influence of the AGN on the physical properties and chemical composition of the CND. Most of them disregard the effects of the UV radiation and consider shocks and/or X-rays irradiation to be the most plausible mechanisms heating the CND (e.g. Galliano & Alloin 2002; Usero et al. 2004; Krips et al. 2011; Hailey-Dunsheath et al. 2012; Spinoglio et al. 2012; Aladro et al. 2013; García-Burillo et al. 2014; Viti et al. 2014). Based on chemical modelling, Viti et al. (2014) have proposed that the CND can be characterized by a three-phase component ISM: two components with enhanced cosmic ray ionization rates by a factor of 10 compared to the MW, and/or X-rays, but with different densities (10^5 and $\geq 10^6\,cm^{-3}$), and a third component dominated by shocks from the outflow driven by the AGN. Our derived H_2 densities of $6 \times 10^5\,cm^{-3}$ for the CND east and $4 \times 10^5\,cm^{-3}$ for the

Downloaded from https://academic.oup.com/mnras/article/502/2/3021/6119921 by guest on 11 February 2026

CND west are in agreement with the densities derived by Viti et al. (2014).

We have found significant lower vibrational temperatures for the CND east and west positions ($T_{\rm vib} \lesssim 75$ K and $\lesssim 114$ K) than the gas kinetic temperatures derived by Viti et al. (2014) (80–160 K and >100 K) and than the vibrational temperature obtained for the SHC ($T_{\rm vib} \sim 240$ K). Furthermore, the rotational temperatures of the CND east and west positions derived from the ground state (49 and 21 K) are also lower than the kinetic temperatures ($T_{\rm rot}$) of the SHC, which is an indication of sub-thermal collisional excitation.

As discussed in Section 4.2, this clearly reflects that the IR pumping is not efficiently exciting HC_3N^* on the CND. This could be due to a low dust optical depth at the wavelength of the vibrational transitions (45 μm for the $v_7 = 1$) or due to a low dust temperature; both effects indicate that the flux of IR photons being re-emitted (i.e. trapping) by dust at 45 μm is small and thus not enough to excite HC_3N^*. The first possibility can be ruled out since the H_2 column densities in the CND are $\sim 10^{24}$ cm^{-2} (see Table 6), which translates to dust opacities at 45 μm of $\tau \sim 16$. Then, the other option is a low dust temperature in the CND in spite of the large luminosity estimated from mid-IR $L_{\rm AGN} \simeq 1.1 \times 10^{11}$ L$_\odot$ (Alonso-Herrero et al. 2011; García-Burillo et al. 2014). This indicates that the dust in the CND remains at a low temperature <100 K (García-Burillo et al. 2014), evidencing that the AGN is not effective at heating the dust in its surroundings. Indeed, as shown below, the upper limit to the dust temperature is consistent with the expected temperature for the heating from the AGN when considering that the dust in the CND is being heated externally. Considering that the CND is a condensation detached from the AGN located at a projected distance from the AGN of ∼75 pc, the expected dust temperature for external heating will be 57 K taking into account the heating for the IR optically thin case using the Stefan–Boltzmann law (de Vicente et al. 2000):

$$T_{\rm d}({\rm K}) = \left(\frac{L}{4\pi\sigma r^2}\right)^{1/4} = 15.222 \left(L({\rm L}_\odot)\left[\frac{10^{16}}{r({\rm cm})}\right]^2\right)^{1/4}. \quad (9)$$

This indicates that the dust in the CND not being efficiently heated by the AGN is due to being externally irradiated by the AGN (i.e. geometrical open system), where photon trapping in the IR is negligible and the temperature profile follows effectively the optically thin case. The opposite happens in geometrical closed systems, where the source is being internally irradiated and is optically thick in the IR. In this case, the greenhouse effect dramatically changes the dust temperature profile in the surrounding material, as observed in the SHC.

The amount of HC_3N^* found in NGC 253 (Rico-Villas et al. 2020) and that found in the NGC 1068 SHC location contrast with its absence in the CND of NGC 1068, where HC_3N column densities are similar to those found in the SHC. While in NGC 253 UV radiation has been found to be the dominant excitation mechanism of H_2 emission (Rosenberg, van der Werf & Israel 2013), in the CND of NGC 1068 it is most likely to be heated by X-ray irradiation (Galliano & Alloin 2002), where gas is also being heated by shocks (García-Burillo et al. 2014; Viti et al. 2014; Kelly et al. 2017).

5.2 History of SF in the SB pseudo-ring of NGC 1068

5.2.1 Ages of SSCs

We can study the recent history of massive SF in the SB pseudo-ring of NGC 1068 by comparing the different tracers presented in this work. As discussed in Rico-Villas et al. (2020), the HC_3N^* emission is thought to be tracing the proto-SSC phase. Then, the free–free radio continuum emission at 147 GHz, arising from ultra-compact H II regions, would be tracing an early phase in the evolution of massive ZAMS stars just after the proto-SSC stage, as seen by their $\alpha_{350-150} > 1$ indexes, and finally, the Pa α emission will be tracing a more evolved phase of massive young stars in the SSCs, as indicated by the lower level of extinction associated with its surrounding material, which is being removed by stellar feedback. In fact, the ratio between the SSC star masses estimated from 147 GHz and from the Pa α emission ($M_{*,147}/M_{*,{\rm Pa}\,\alpha}$) can be used to make a rough estimate of the evolutionary stage of the SSCs. The $M_{*,147}/M_{*,{\rm Pa}\,\alpha}$ mass ratio is expected to be close to 1 for no extinction, and it will increase as the extinction increases, since with the continuum emission at 147 GHz we are seeing a more embedded phase of SF. This is indeed the trend found in the $M_{*,147}/M_{*,{\rm Pa}\,\alpha}$ ratio in Table 7. We can see that the SSCs with the lowest values of about 1, SSC 1, SSC 2, Pa α 1, and Pa α 2, almost do not show dust continuum emission at 350 GHz, as expected for low extinction. It is worth to remark that we are focusing on specific clumps in the SB pseudo-ring where the dust continuum emission at 350 GHz peaks (except for the Pa α 1 and 2 sources) and hence the Pa α emission is expected to suffer some extinction, although it seems to have no extinction outside these clumps (for a more detailed analysis on the Pa α emission in the SB pseudo-ring, see Sánchez-García et al., in preparation). The highest values of the $M_{*,147}/M_{*,{\rm Pa}\,\alpha}$ ratios correspond to the proto-SSC (i.e. the SHC) and the SSC 6 located in the northern region of the SB pseudo-ring. The high value found in the proto-SSC is consistent with the very early stage of the SSC formation. Following the procedure described by Rico-Villas et al. (2020), we can use the ratio of the mass in protostars ($M_{\rm p*}$) to the mass in ZAMS stars ($M_{*,147}$), to make an estimation of their age assuming that protostars have a time-scale of $\lesssim 10^5$ yr with

$$t_{\rm age}({\rm yr}) \sim \frac{1}{1 + M_{\rm p*}/M_{*,147}} \times 10^5. \quad (10)$$

The estimated age of the proto-SSC is 5.8×10^4 yr. For the more evolved SSCs without detected HC_3N^* emission, we can estimate their ages using the ratio $M_{*,147}/M_{*,{\rm Pa}\,\alpha}$. Assuming that the feedback from the SSCs removes the leftover material from cluster formation in $\sim 10^7$ yr (Dowell, Buckalew & Tan 2008) and assuming a linear dependence of the gas removal with age, we can estimate the age as

$$t_{\rm age,Pa}({\rm yr}) = \frac{1}{1 + 13 \cdot (M_{*,147}/M_{*,{\rm Pa}\,\alpha} - 1)} \times 10^7, \quad (11)$$

where 13 is a scale factor obtained from the SHC position so its $t_{\rm age,p*} = t_{\rm age,Pa}$. The ages obtained are listed in Table 7. We find that the youngest SSCs are the SHC and SSC 6 (ages of 6×10^4 yr) located in the northern part of the SB pseudo-ring, and SSC 7, 8, 9, and 11 [ages of $(2–4) \times 10^5$ yr] in the southern part of the SB pseudo-ring. It is remarkable that the SSCs seem to be closely associated with the nuclear stellar bar and the beginning of the molecular spiral arms.

We can use the gas mass obtained from the 350 GHz continuum emission to make an estimation of the star formation efficiency (SFE; Table 7) by assuming that the initial mass of the star-forming molecular clouds has not suffered significant mass-losses. Since we only have upper limits for $M_{\rm p*}$ for most of the SSCs, we will use only $M_{*,147}$ and the expression

$${\rm SFE} = \frac{1}{1 + M_{\rm gas}/M_{*,147}}. \quad (12)$$

In case that mechanical feedback has played a significant role, like in the case of Pa α 1 and 2, the SFE must be considered as an upper limit.

Downloaded from https://academic.oup.com/mnras/article/502/2/3021/6119921 by guest on 11 February 2026

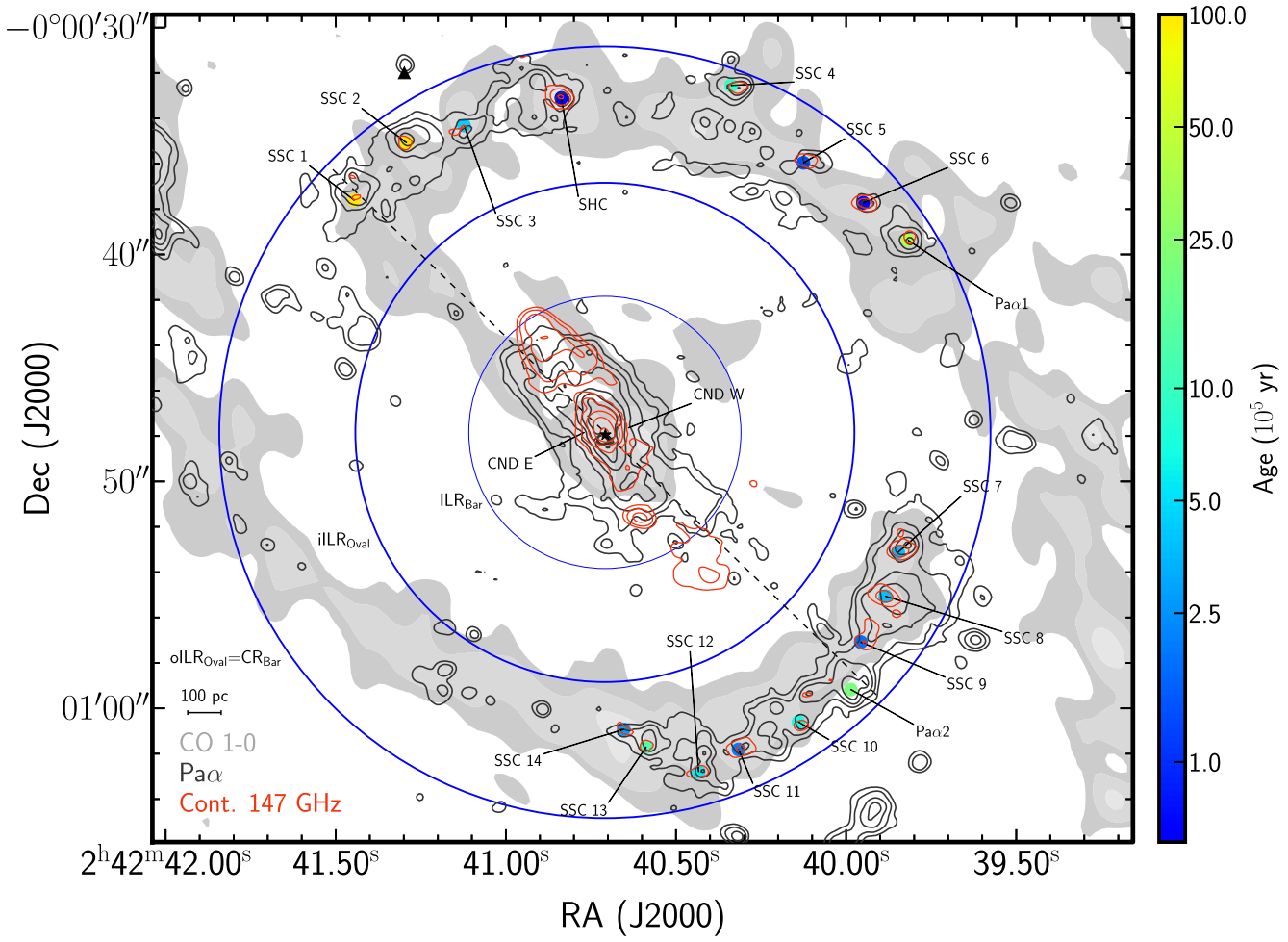


Figure 5. NGC 1068 map as seen by CO 1–0 (grey scale), Pa α (black contours), and continuum emission at 147 GHz (red contours). The SB pseudo-ring is clearly seen in CO and Pa α emission. The AGN position is marked with a star. Type II SN 2018ivc position is marked with a triangle (Bostroem et al. 2020). The stellar bar is indicated with a straight dashed black line. The ILRs from the outer oval and the stellar bar (Schinnerer et al. 2000; García-Burillo et al. 2010) are indicated by solid blue lines, respectively. The estimated ages ($t_{\rm Age,Pa}$) for the different positions are colour coded following the colour wedge on the right.

The SFE of the proto-SSC is only 0.2, suggesting that the SF is very recent and still has a significant amount of gas available to convert into stars. SSCs 6, 7, 8, 9, and 11, with ages of few 10^5 yr, seem to be in a similar state to the SHC, where the latest SF episode is just starting (or has just concluded). Unfortunately, the lack of sensitivity to detect HC_3N^* does not allow us to discriminate between the two possibilities. SSC 2 shows a relatively high gas mass and a relatively low SFE, but seems to be rather evolved as its $M_{*,147}/M_{*,{\rm Pa}\,\alpha}$ ratio suggests. This could indicate that its SF has been halted and a next generation of stars could be forming in an unrelated giant molecular cloud unresolved by our observations. On the other hand, SSC 1 has an SFE $\lesssim 0.5$ with low $M_{\rm gas}$, indicating that it has already formed most of its stars.

5.2.2 *Propagation of SSC formation in the ring*

NGC 1068 is a classical case of two embedded bars that have resonances in common: the large-scale stellar oval of length ∼17 kpc (Telesco & Decher 1988; Schinnerer et al. 2000) and the nuclear stellar bar of $r \sim 1.3$ kpc and a position angle of 46° (Scoville et al. 1988; Schinnerer et al. 2000). The large-scale oval has its corotation at $R_{\rm cor} = 120$–140 arcsec ~ 8.5–10 kpc (see Schinnerer et al. 2000), while the nuclear stellar bar corotation is at $R_{\rm cor} = 15$–2 arcsec $\sim$ 1–1.5 kpc. This corotation of the nuclear bar coincides with the outer Inner Lindblad Resonance (oILR) of the large-scale oval. These overlapping resonances favour the decoupling of the nuclear bar from the large-scale bar. There is a tightly wound nuclear spiral in the gas ('the SB pseudo-ring') that is identified by the accumulation of molecular gas (seen in CO in Fig. 5) in a pseudo-ring at radii (r) of 15–20 arcsec, i.e. at the corotation of the nuclear bar. The formation of a pseudo-ring is a natural consequence of the gas responding to the dynamical resonances induced by a bar-shaped potential. The CO arms are at the nuclear bar corotation radius, indicating that the gas is responding to the larger scale oval in NGC 1068, which would favour inflows to its ILR (García-Burillo et al. 2014).

Assuming that gas rotation in NGC 1068 is counter-clockwise if the spiral arms are trailing, the CO ridge appears 'upstream' (i.e. at shorter radii, on the inner face of the spiral arm) along the expected gas circulation lines, while the SF tracers (both Pa α and 147 GHz continuum) tend to appear 'downstream' (i.e. at longer radii, on the outer face of the spiral arm). This is the expected 'sequence' if the gas is responding to the spiral inside corotation: It enters the spiral arm, where it is being accumulated and/or compressed and then SF is triggered. An example of this sequence is seen in M 51 spiral arms

Downloaded from https://academic.oup.com/mnras/article/502/2/3021/6119921 by guest on 11 February 2026

(Louie, Koda & Egusa 2013). If we zoom in the SB pseudo-ring, one would also expect to see the older SF (i.e. the Pa α emission) downstream relative to the younger and still embedded SF (i.e. the 147 GHz continuum and/or the HC_3N^*). Hints of this intricate 'subsequence' can be found on the SW region but is less clear on the NE region.

A sizeable fraction of the massive recent SF is concentrated in two regions located NE and SW along PA = 46°, where the CO spiral arms join with the end of the nuclear bar (see Fig. 5). These are the regions where García-Burillo et al. (2014) identified strong non-circular motions revealing an inflow and where the orbit families of the spiral and the bar are expected to cross, which would favour cloud–cloud collisions that enhance the SF. Beuther et al. (2017) observed a similar build of resonances in NGC 3627 that pile up the gas where the different orbit families cross, favouring strong SF events. This is also occurring in the MW, where the overlap between the end of the Galactic bar with the spiral arm hosts the W43 starburst region (see Beuther et al. 2017, and references therein).

Despite the inflow gas motions that lead to the molecular gas pile-up in the spiral arms, SF is not uniformly distributed throughout the entire SB pseudo-ring: The two contact-point regions located SW and NE stand out as the sites where the bulk of the recent and massive SF is taking place. However, if we consider the different SSC ages (from Table 7) and their projected location relative to the nuclear bar (Fig. 6), it seems that there is no ordered sequence of the star-forming regions inside these two regions. This would be in accordance with the 'popcorn' scenario instead of the 'pearls on a string' scenario described by Böker et al. (2008). In the 'popcorn' scenario, the star-forming regions would appear at random times and locations within the pseudo-ring and there would be no systematic sequence of SF along the pseudo-ring. The collection of different initial conditions of each cloud when they enter the spiral arm would make the triggering of the SF appear at random times.

5.3 HC_3N^* as a discriminator between AGN and SF activity in galaxies

The different excitation mechanism present in the CND, where no recent SF is taking place (last starburst was 200–300 Myr ago; Davies et al. 2007), compared to those observed in the young star-forming regions where HC_3N^* has been observed, suggests that HC_3N^* could be used as a discriminator between AGN and early obscured SF activity in galaxies.

So far, HC_3N^* has been detected in two active galaxies, the LIRG NGC 4418, located at 35.8 Mpc with $L_{IR} = 1.5 \times 10^{11}$ L$_\odot$ (Costagliola & Aalto 2010), and the ULIRG Arp 220 (Martín et al. 2011), located at 79.4 Mpc with $L_{IR} = 1.5 \times 10^{12}$ L$_\odot$. For both galaxies, the origin of the high IR luminosity (AGN versus SB) is highly debated due to the extremely large extinctions. For NGC 4418, Sakamoto et al. (2013) favoured the heating by a Compton-thick AGN, but Varenius et al. (2014) claimed to be SB dominated. A similar controversy also exists for Arp 220 (e.g. Sakamoto et al. 1999; Wilson et al. 2014; Barcos-Muñoz et al. 2015; Sakamoto et al. 2017).

Following the results found for the CND, we can compare the estimated T_{vib}, HC_3N^* brightness temperature, and source sizes for NGC 4418 and Arp 220. Using results from previous works, we can compare between the sizes derived from HC_3N^* emission and those predicted from equation (9) to discriminate between obscured AGN and SF scenarios. For NGC 4418, Costagliola et al. (2015) estimated a $T_{vib} = 340$ K, with a brightness temperature in the $J =$ 24–23, $v_7 = 1$f line of 9 K for a source size of 0.4 arcsec (69 pc).

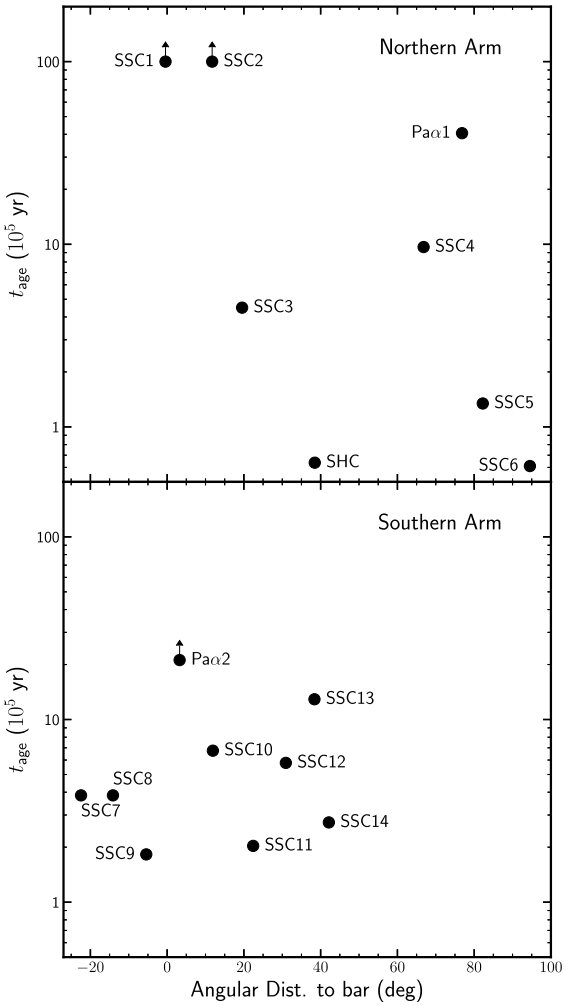


Figure 6. SSC ages as a function of their relative distance to the nuclear bar. Top panel shows the SSCs on the northern spiral arm. Bottom panel shows the SSCs on the southern spiral arm.

Assuming optically thick emission for that line, we derive a lower limit to the size of ∼0.07 arcsec (∼12 pc). For Arp 220, Martín et al. (2011) measured for the $J = 25$–24, $v_7 = 1$f line a mean beam brightness temperature of 263.9 mK in an 8.4 arcsec × 6.1 arcsec beam and estimated a $T_{vib} \sim 355$ K. Applying the same procedure as for NGC 4418, we derive a lower limit to the HC_3N^* emission of ∼0.2 arcsec (∼80 pc) for Arp 220.

Taking into account the results obtained for the heating of the CND by the AGN in NGC 1068 (equation 9), one would expect the size of the region emitting the bulk of the hot gas (∼340 K) observed in HC_3N^* for NGC 4418 and Arp 220 to be about 2.5 and 8.0 pc, respectively (i.e. 0.015 and 0.021 arcsec), if the heating is dominated by a central source as expected for an AGN. The predicted sizes by equation (9) are clearly much smaller than the measured lower limits to the sizes of the HC_3N^* emission in both sources. The rather small predicted sizes for the dust region heated by the AGN would indicate that the heating is instead distributed over the large region observed in HC_3N^* due to SF as observed in the NGC 1068 SB pseudo-ring.

However, as discussed in Section 5.1, equation (9) can only be applied to predict the dust temperature profile for the case of an optically thin cloud (open systems) in the IR. González-Alfonso & Sakamoto (2019) have studied in detail the dust temperature profile

Downloaded from https://academic.oup.com/mnras/article/502/2/3021/6119921 by guest on 11 February 2026

due to the heating by an AGN and an SB in a spherical cloud considering the back warming effect due to extremely high extinction (i.e. closed systems) as observed in NGC 4418 and Arp 220. They found that for a luminosity surface brightness of (1–2) $\times$ 10^8 $L_\odot$ pc^{-2} for NGC 4418 and Arp 220 and an H_2 column density of 10^{25} cm^{-2}, the size of the region with $T_d > 300$ K is about 20 and 100 pc for NGC 4418 and Arp 220, respectively, basically independent of the nature of the heating source. Therefore, discriminating between AGN and SB heating using HC_3N^* emission in IR optically thick galaxy nuclei can only be done when the spatial resolution is high enough to measure the T_{vib} profile close to the central heating source, where the temperature gradient is expected to show the largest difference between the AGN and SB heating.

6 SUMMARY AND CONCLUSIONS

We have used the archival ALMA data to study the HC_3N emission from its ground and vibrationally excited states, along with the 147 GHz continuum emission, in the SB pseudo-ring and in the CND of NGC 1068. The main results can be summarized as follows:

(i) We have detected emission from HC_3N (lines $J = 11$–10, 12–11, 16–15, and 24–23) in the ground state towards the SB pseudo-ring and the CND. In spite of the bright HC_3N emission observed towards the CND east, we did not detect any vibrationally excited emission. In contrast, vibrationally excited emission from the $v_7 = 1$e and 1f lines ($J = 16$–15 and 24–23) of HC_3N was detected towards one star-forming region on the northern part of the SB pseudo-ring.

(ii) For the star-forming region in the SB pseudo-ring with HC_3N^* emission, the LTE analysis yields a vibrational temperature (T_{vib}) between the $v = 0$ and $v_7 = 1$ levels of 236 $\pm$ 18 K and a rotational temperature, T_{rot}, between the rotational levels in the ground state of 98 $\pm$ 7 K. The difference in excitation temperatures suggests that the vibrational levels are excited by IR pumping at the dust temperature while the rotational levels are collisionally excited. This is consistent with the derived T_{dust} and H_2 densities from our non-LTE analysis of 248 $\pm$ 28 K and (5.9 $\pm$ 0.2) $\times$ 10^5 cm^{-3}, respectively. The latter indicates that we are observing an SHC similar to those observed in NGC 253 (Rico-Villas et al. 2020).

(iii) From the dust temperature and the lower limit to the size of the SHC in the SB pseudo-ring, we estimated an IR luminosity of $\sim$5.8 $\times$ 10^8 $L_\odot$, typical of the proto-superstar clusters (proto-SSCs) observed in NGC 253, which are believed to be tracing the earliest phase of the SSC formation.

(iv) In addition to the SHC, we have also identified from our continuum map at 147 GHz another 14 young star-forming regions undergoing the H II region phase in the SB pseudo-ring. Assuming that the continuum is dominated by free–free emission, we have obtained the stellar mass of ZAMS massive stars for the regions in the SB pseudo-ring. These embedded star-forming regions contain stellar masses of $\sim$$10^5$ $M_\odot$, typical of SSCs and proto-SSCs. Unfortunately, our sensitivity on the HC_3N^* emission is not high enough to discard the presence of the proto-SSC phase.

(v) We have also used the Pa α emission to trace a more evolved SF phase in the SB pseudo-ring. We combined the tracers of the different evolutionary phases to estimate the ages of the SSCs, which range from few 10^4 yr for the proto-SSCs to 10^7 yr for the most evolved SSCs with little extinction as derived from the ratio of the Pa α to 147 GHz derived stellar masses and the lack of dust/CO emission.

(vi) The SSC location and derived young ages are closely associated with the region connecting the nuclear bar with the SB pseudo-ring, where most of the gas is being accumulated and an increase of cloud–cloud collisions is expected. The most recent and still embedded SF episodes would be taking place in this region, as expected in the scenario of the inflow scenario. We do not find any systematic trend of the ages of the SSCs within the ring, supporting the 'popcorn' mode of SF.

(vii) For the CND east and west positions, our LTE and non-LTE analyses of HC_3N emission yield an upper limit to T_{vib} of $\leq$98 and $\leq$117 K and a T_{rot} of 41 $\pm$ 1 and 29 $\pm$ 3 K, respectively. The derived H_2 densities are (5.9 $\pm$ 0.3) $\times$ 10^5 and (3.5 $\pm$ 0.5) $\times$ 10^5 cm^{-3}.

(viii) The low dust temperature $<$100 K derived towards the CND is consistent with the expected heating by the AGN in NGC 1068 for a luminosity of 1.1 $\times$ 10^{11} $L_\odot$ considering the IR optically thin case and that the dust in the CND is being externally heated (open system). The opposite happens in the SHC, which is being internally irradiated by the forming protostars and is optically thick in the IR (closed system).

(ix) We discussed whether, as observed in NGC 1068, the HC_3N^* emission observed in NGC 4418 and Arp 220 can be used to discriminate between AGN and SB activity. We concluded that just the detection of HC_3N^* emission cannot be used as a discriminator because the greenhouse effect in heavily obscured galactic nuclei (closed systems) makes the AGN and SB dust profiles to be similar at large distances. Only the combination of spatially resolved images of several HC_3N^* lines might provide the insight for the discrimination.

ACKNOWLEDGEMENTS

This paper makes use of the ALMA data listed in Table 1. ALMA is a partnership of ESO (representing its member states), NSF (USA), and NINS (Japan), together with NRC (Canada), NSC and ASIAA (Taiwan), and KASI (Republic of Korea), in cooperation with the Republic of Chile. The Joint ALMA Observatory is operated by ESO, AUI/NRAO, and NAOJ.

The Spanish Ministry of Science and Innovation has supported this research under grant number ESP2017-86582-C4-1-R, PhD fellowship BES-2016-078808, and MDM-2017-0737 Unidad de Excelencia María de Maeztu.

VMR acknowledges support from the Comunidad de Madrid through the Atracción de Talento Investigador Senior Grant (COOL: Cosmic Origins Of Life; 2019-T1/TIC-15379), and from the European Union's Horizon 2020 research and innovation programme under the Marie Skłodowska-Curie grant agreement number 664931.

IJS has received partial support from the Spanish European Regional Development Fund (FEDER; project number ESP2017-86582-C4-1-R) and the State Research Agency (AEI; project number PID2019-105552RB-C41).

DATA AVAILABILITY

The data underlying this article were accessed from the ALMA Science Archive (http://almascience.eso.org/asax/), with the corresponding project identifiers listed in Table 1. The derived data generated in this research will be shared on reasonable request to the corresponding author.

REFERENCES

Aalto S., 2015, in Daisuke I., Ken-ichi T., Alwyn W., Leonardo T., eds, ASP Conf. Ser. Vol. 499, Revolution in Astronomy with ALMA: The Third Year. Astron. Soc. Pac., San Francisco, p. 85

Aladro R., Viti S., Riquelme D., Martín S., Mauersberger R., Martín-Pintado J., Bayet E., 2012, J. Phys. Conf. Ser., 372, 012039

Downloaded from https://academic.oup.com/mnras/article/502/2/3021/6119921 by guest on 11 February 2026

Aladro R. et al., 2013, A&A, 549, A39
Alonso-Herrero A. et al., 2011, ApJ, 736, 82
Anantharamaiah K. R., Zhao J.-H., Goss W. M., Viallefond F., 1993, ApJ, 419, 585
Barcos-Muñoz L. et al., 2015, ApJ, 799, 10
Beck S., 2015, Int. J. Mod. Phys. D, 24, 1530002
Beuther H., Meidt S., Schinnerer E., Paladino R., Leroy A., 2017, A&A, 597, A85
Bland-Hawthorn J., Gallimore J. F., Tacconi L. J., Brinks E., Baum S. A., Antonucci R. R. J., Cecil G. N., 1997, Ap&SS, 248, 9
Böker T., Falcón-Barroso J., Schinnerer E., Knapen J. H., Ryder S., 2008, AJ, 135, 479
Bostroem K. A. et al., 2020, ApJ, 895, 31
Combes F. et al., 2019, A&A, 623, A79
Costagliola F., Aalto S., 2010, A&A, 515, A71
Costagliola F., Aalto S., Sakamoto K., Martín S., Beswick R., Muller S., Klöckner H. R., 2013, A&A, 556, A66
Costagliola F. et al., 2015, A&A, 582, A91
Davies R. I., Müller Sánchez F., Genzel R., Tacconi L. J., Hicks E. K. S., Friedrich S., Sternberg A., 2007, ApJ, 671, 1388
Davis B. L. et al., 2014, ApJ, 789, 124
DeLeon R. L., Muenter J. S., 1985, J. Chem. Phys., 82, 1702
de Vicente P., Martín-Pintado J., Neri R., Colom P., 2000, A&A, 361, 1058
de Vicente P., Martín-Pintado J., Neri R., Rodríguez-Franco A., 2002, ApJ, 574, L163
Donnison J. R., Williams I. P., 1976, Nature, 261, 674
Dowell J. D., Buckalew B. A., Tan J. C., 2008, AJ, 135, 823
Galliano E., Alloin D., 2002, A&A, 393, 43
García-Burillo S. et al., 2010, A&A, 519, A2
García-Burillo S. et al., 2014, A&A, 567, A125
García-Burillo S. et al., 2017, A&A, 608, A56
García-Burillo S. et al., 2019, A&A, 632, A61
Genzel R. et al., 1998, ApJ, 498, 579
Goldsmith P. F., Langer W. D., 1999, ApJ, 517, 209
Goldsmith P. F., Snell R. L., Deguchi S., Krotkov R., Linke R. A., 1982, ApJ, 260, 147
González-Alfonso E., Cernicharo J., 1997, A&A, 322, 938
González-Alfonso E., Cernicharo J., 1999, ApJ, 525, 845
González-Alfonso E., Sakamoto K., 2019, ApJ, 882, 153
González-Alfonso E. et al., 2012, A&A, 541, A4
González-Alfonso E., Fischer J., Aalto S., Falstad N., 2014, A&A, 567, A91
Hailey-Dunsheath S. et al., 2012, ApJ, 755, 57
Hosokawa T., Omukai K., 2009, ApJ, 691, 823
Imanishi M., Nakanishi K., Izumi T., 2016, ApJ, 822, L10
Imanishi M., Nakanishi K., Izumi T., 2019, ApJS, 241, 19
Jiménez-Serra I., Martín-Pintado J., Caselli P., Martín S., Rodríguez-Franco A., Chandler C., Winters J. M., 2009, ApJ, 703, L157
Kelly G., Viti S., García-Burillo S., Fuente A., Usero A., Krips M., Neri R., 2017, A&A, 597, A11
Kennicutt Robert C. J., 1998, ARA&A, 36, 189
Krips M., Eckart A., Neri R., Schödel R., Leon S., Downes D., García-Burillo S., Combes F., 2006, A&A, 446, 113
Krips M. et al., 2011, ApJ, 736, 37
Leroy A. K. et al., 2018, ApJ, 869, 126
Louie M., Koda J., Egusa F., 2013, ApJ, 763, 94
Lusso E. et al., 2013, ApJ, 777, 86
McMullin J. P., Waters B., Schiebel D., Young W., Golap K., 2007, in Shaw R. A., Hill F., Bell D. J., eds, ASP Conf. Ser. Vol. 376, Astronomical Data Analysis Software and Systems XVI. Astron. Soc. Pac., San Francisco, p. 127
Martín S. et al., 2011, A&A, 527, A36
Martín S., Martín-Pintado J., Montero-Castaño M., Ho P. T. P., Blundell R., 2012, A&A, 539, A29
Martín S. et al., 2016, A&A, 590, A25
Martín S., Martín-Pintado J., Blanco-Sánchez C., Rivilla V. M., Rodríguez-Franco A., Rico-Villas F., 2019, A&A, 631, A159
Martín-Pintado J., Jiménez-Serra I., Rodríguez-Franco A., Martín S., Thum C., 2005, ApJ, 628, L61
Müller H. S. P., Thorwirth S., Roth D. A., Winnewisser G., 2001, A&A, 370, L49
Müller H. S. P., Schlöder F., Stutzki J., Winnewisser G., 2005, J. Mol. Struct., 742, 215
Müller-Sánchez F., González-Martín O., Fernández-Ontiveros J. A., Acosta-Pulido J. A., Prieto M. A., 2010, ApJ, 716, 1166
Murphy E. J. et al., 2011, ApJ, 737, 67
Osterbrock D. E., Ferland G. J., 2006, Astrophysics of Gaseous Nebulae and Active Galactic Nuclei, 2nd edn. Univ. Sci. Books, Sausalito, CA
Piqueras López J., Colina L., Arribas S., Pereira-Santaella M., Alonso-Herrero A., 2016, A&A, 590, A67
Rico-Villas F., Martín-Pintado J., González-Alfonso E., Martín S., Rivilla V. M., 2020, MNRAS, 491, 4573
Rosenberg M. J. F., van der Werf P. P., Israel F. P., 2013, A&A, 550, A12
Sakamoto K., Scoville N. Z., Yun M. S., Crosas M., Genzel R., Tacconi L. J., 1999, ApJ, 514, 68
Sakamoto K., Aalto S., Evans A. S., Wiedner M. C., Wilner D. J., 2010, ApJ, 725, L228
Sakamoto K., Aalto S., Costagliola F., Martín S., Ohyama Y., Wiedner M. C., Wilner D. J., 2013, ApJ, 764, 42
Sakamoto K. et al., 2017, ApJ, 849, 14
Schinnerer E., Eckart A., Tacconi L. J., Genzel R., Downes D., 2000, ApJ, 533, 850
Scoville N. Z., Matthews K., Carico D. P., Sand ers D. B., 1988, ApJ, 327, L61
Spinoglio L. et al., 2012, ApJ, 758, 108
Sternberg A., Genzel R., Tacconi L., 1994, ApJ, 436, L131
Tacconi L. J., Genzel R., Blietz M., Cameron M., Harris A. I., Madden S., 1994, ApJ, 426, L77
Telesco C. M., Decher R., 1988, ApJ, 334, 573
Telesco C. M., Harper D. A., 1980, ApJ, 235, 392
Turner J. L., Ho P. T. P., 1985, ApJ, 299, L77
Usero A., García-Burillo S., Fuente A., Martín-Pintado J., Rodríguez-Fernández N. J., 2004, A&A, 419, 897
Varenius E., Conway J. E., Martí-Vidal I., Aalto S., Beswick R., Costagliola F., Klöckner H. R., 2014, A&A, 566, A15
Viti S. et al., 2014, A&A, 570, A28
Whitmore B. C., Schweizer F., 1995, AJ, 109, 960
Wilson C. D. et al., 2008, ApJS, 178, 189
Wilson C. D., Rangwala N., Glenn J., Maloney P. R., Spinoglio L., Pereira-Santaella M., 2014, ApJ, 789, L36
Wyrowski F., Schilke P., Walmsley C. M., 1999, A&A, 341, 882

This paper has been typeset from a TEX/LATEX file prepared by the author.

Downloaded from https://academic.oup.com/mnras/article/502/2/3021/6119921 by guest on 11 February 2026